Dalton Transactions

ROYAL SOCIETY OF CHEMISTRY

PAPER

View Article Online
View Journal | View Issue

Cite this: *Dalton Trans.*, 2025, **54**, 14304

Nanoscale ruthenium(III) complexes with bioactive ligands: structural, colloidal, and dual antimicrobial–cytotoxic investigations†

Olga Impert,*[a] Natalia Czerniecka,[a] Natalia Balińska,[a] Barbara Kubiak,[a] Anna Kozakiewicz-Piekarz,[a] Oleksandra Pryshchepa,[b] Paweł Pomastowski,[b] Michalina Ehlert,[b] Maciej Witwicki,[d] Yogeswara Rao Pateda,[a,e] Erik Rakovský,[e] Anna Katafias[a] and Rudi van Eldik[*a,c]

This study comprehensively analyses two new ruthenium(III) complexes, $[Ru^{III}Cl_4(Nic)_2]^-[(CH_3)_2NH_2]^+DMF$, **1**, and $[Ru^{III}Cl_2(3\text{-}HPA)_2]^-[3\text{-}HH_2PA]^+(EtOH)_2$, **2**, (where Nic = nicotinic acid (vitamin B3), 3-HPA = anion of a 3-hydroxypicolinic acid), as potential antimicrobial agents, highlighting their physicochemical properties, nanoparticle formation, and cytotoxic activity. The complexes were fully characterised by a single crystal X-ray diffraction technique, Fourier-transform infrared, energy-dispersive X-ray, and electron paramagnetic resonance spectroscopies. The synthesis of micro- and nanoparticles (NPs) of these complexes was performed using the liquid anti-solvent crystallisation method. The formation of NPs was confirmed, and their sizes were determined using scanning electron microscopy and dynamic light scattering techniques. The Debye-Scherrer technique, based on powder diffraction X-ray data, indicated the high crystallinity of the nanomaterials. Toxicity and morphological effects on L929 fibroblasts, hepatocellular carcinoma (Hep-G2) and human epithelial colorectal adenocarcinoma (Caco-2) cell lines of the complexes were assessed using the MTT assay and an inverted phase-contrast microscope, respectively. Complex **1** is a promising anti-cancer drug candidate targeting intestinal cancers, showing cytotoxicity against Caco-2 cancer cells and no cytotoxicity against L929 fibroblast cells, while complex **2** is markedly cytotoxic. The antibacterial activity of the complexes was assessed against methicillin-resistant *Staphylococcus aureus* (MRSA) and *Klebsiella pneumoniae* strains using the minimum inhibitory concentration (MIC) method. Complex **2** demonstrates superior bactericidal properties, achieving MIC values as low as 125 μg ml^{-1} for *S. aureus*, while complex **1** exhibits lower antimicrobial efficacy. The role of ligand composition in modulating bioactivity was examined.

Received 3rd August 2025,
Accepted 15th August 2025

DOI: 10.1039/d5dt01857a

rsc.li/dalton

Introduction

One of the most pressing global health challenges today is the rise of antibiotic-resistant bacterial strains. The common over- and misuse of conventional antibiotics have led to an alarming increase in bacterial resistance, rendering many commonly used drugs ineffective. Consequently, the spread of antibiotic-resistant bacteria, both Gram-positive and Gram-negative, is of great concern worldwide. A significant threat to human health poses Gram-positive methicillin-resistant *Staphylococcus aureus* (MRSA), responsible for difficult-to-treat hospital- and community-acquired infections, especially strains resistant to vancomycin, linezolid and daptomycin.[1] A very concerning form of antimicrobial resistance is carbapenemase-mediated resistance to carbapenems, one of the most recently developed β-lactam antibiotics, often known as a last-resort treatment for severe bacterial infections.[2] The worldwide spread of carbapenemase-producing Gram-negative bacteria, such as *Klebsiella pneumoniae*, an important pathogen in nosocomial infections, is another therapeutic challenge. This crisis necessitates urgently exploring alternative therapeutic strategies to overcome resistance mechanisms and effectively target pathogenic microorganisms. The search for antibacterial agents includes metal ions, transition metal-based complex nanoparticles,

[a]*Faculty of Chemistry, Nicolaus Copernicus University in Toruń, Gagarina 7, 87-100 Toruń, Poland. E-mail: oimpert@umk.pl, rudi.vaneldik@umk.pl*
[b]*Centre for Modern Interdisciplinary Technologies, Nicolaus Copernicus University in Toruń, Wileńska 4, 87-100 Toruń, Poland*
[c]*Department of Chemistry and Pharmacy, University of Erlangen-Nuremberg, Egerlandstrasse 1, 91058 Erlangen, Germany*
[d]*Faculty of Chemistry, University of Wroclaw, Joliot-Curie 14, 50-383 Wroclaw, Poland*
[e]*Comenius University in Bratislava, Faculty of Natural Sciences, Department of Inorganic Chemistry, Ilkovičova 6, 845 15 Bratislava, Slovakia*
†This work is to honour Professor Dr Rudi van Eldik on the occasion of his 80th birthday.

metal complexes with antimicrobial activity, and catalytic metallodrugs.[3] They constitute a large and insufficiently studied group of compounds that may create a much-needed new class of antibacterials.

Transition metal-based complexes have been explored for their antimicrobial properties, including copper, gallium, zinc, manganese, silver, gold, and ruthenium. Their mode of action differs from that of organic-based drugs. When coordinated with bioactive ligands, these metal ions exhibit enhanced antimicrobial activity due to their ability to interfere with bacterial metabolism, disrupt membrane integrity, and generate reactive oxygen species (ROS), leading to bacterial cell death.[4] Among the transition metal complexes, ruthenium-based compounds have garnered significant attention in medicinal chemistry due to their diverse oxidation states (II, III, IV) and ability to interact with biological molecules in a highly selective manner. Their favourable ligand exchange kinetics, capacity to mimic iron in biological systems, and ability to participate in redox reactions under physiological conditions make them promising candidates for therapeutic applications, including antimicrobial treatments. Ruthenium complexes have demonstrated potent cytotoxic activity through multiple pathways, including extracellular protein binding, passive and active cellular transport, DNA intercalation, and covalent modifications at extracellular binding sites, leading to conformational changes in bacterial biomolecules.[5–11] These properties position ruthenium complexes not only as alternative anti-tumour drugs but also as a strong contender in developing next-generation antimicrobial agents. Although their cytotoxic activity and cellular localisation in eukaryotic cells have been intensively studied over the past few decades, the thorough investigation of the antimicrobial properties of ruthenium complexes has been undertaken much more recently. It is still in its early stages, despite the observation of Dwyer *et al*. that bacteria did not readily develop resistance to ruthenium complexes containing methyl substituents of phenanthroline ligands.[12] Aldrich-Wright and co-workers reported that mononuclear polypyridyl ruthenium(II) complexes, which could bind DNA, showed significant bactericidal activity against *B. subtilis* and *S. aureus* strains, including several methicillin-resistant strains. Some complexes even showed MIC values as low as 2 μg ml^{-1} against Gram-positive strains.[13] Lam *et al*. recently showed good activity of bis(2,2′-bipyridine)-ruthenium(II) complexes containing an *N*-phenyl-substituted diazafluorene ligand against MRSA (6.25 μg ml^{-1}), bis(2,2′-bipyridine)-ruthenium(II) complexes containing an *N*-phenyl-substituted diazafluorene ligand.[14] Satyanarayana *et al*. also found that a series of mononuclear ruthenium complexes containing derivatives of the dipyridophenazine or 2-phenylimidazo-1,10-phenanthroline ligands showed moderate activity.[11] Considering the above, research on new antibacterial agents, including those based on ruthenium, has become urgent. We herein report the design and syntheses of two complexes: $[Ru^{III}Cl_4(Nic)_2]^-[(CH_3)_2NH_2]^+DMF$, **1**, and $[Ru^{III}Cl_2(3\text{-}HPA)_2]^-[3\text{-}HH_2PA]^+(EtOH)_2$, **2**, and their antibacterial activity against *Klebsiella pneumoniae* and *Staphylococcus aureus* strains. We also prepared nanoparticles of these complexes using the liquid antisolvent crystallisation (LASC) method. It is known that nanoparticles, due to their small size and large surface area, can attach to the cell wall of bacteria and cause cell death.[15–20] The latest endeavour is a foray into nanoparticle-based antibiotic research to address the limitations of current antibacterial drugs.

Experimental

Materials and methods

All chemicals were of analytical reagent grade and used without further purification. Ruthenium(III) chloride, nicotinic acid, and 3-hydroxypicolinic acid were purchased from Sigma-Aldrich. Acetone, *n*-hexane, toluene, DMF, nitrobenzene, ethanol, chloroform, acetonitrile, ethyl acetate, diethyl ether, isopropyl alcohol, isobutyl alcohol, cyclohexane, and methanol were purchased from Avantor Performance Materials Poland. Hydrogen peroxide solutions were prepared by diluting a 30% solution (Avantor Performance Materials Poland S.A.).

$[Ru^{III}Cl_4(Nic)_2]^-[(CH_3)_2NH_2]^+DMF$, 1. 7 mmol of ruthenium (III) chloride and 60 ml of anhydrous ethyl alcohol were heated under reflux for 3 hours. The solution was filtered while hot. 14 mmol of nicotinic acid was added, and heating continued for 7 hours until the colour changed from green to brown, and a yellow precipitate formed. The resulting hot mixture was filtered, and the residue was washed 3 times with anhydrous ethanol and recrystallised from a mixture of DMF and nitrobenzene (2 : 1). Brown crystals of **1** were obtained. Elemental Anal. Calc. for $C_{20}H_{32}Cl_4N_5O_6Ru_1$: C, 35.24%; N, 10.28%; H, 4.73%. Found: C, 35.35%; N, 10.20%; H, 4.69%.

$[Ru^{III}Cl_2(3\text{-}HPA)_2]^-[3\text{-}HH_2PA]^+(EtOH)_2$, 2. 2.4 mmol of ruthenium(III) chloride in 30 ml of anhydrous ethyl alcohol was heated for 3 hours under reflux (green colour of the solution), then filtered while hot. 12.6 mmol of 3-hydroxypicolinic acid was added, and heating continued for 1 hour (yellow–brown solution). The mixture was filtered while hot, and the precipitate was recrystallised from 96% ethanol and water (1 : 1). The Yellow crystals of **2** were obtained. Elemental Anal. Calc. for $C_{22}H_{26}Cl_2N_3O_{11}Ru_1$: C, 38.84%; N, 6.18%; H, 3.85%. Found: C, 38.80%; N, 6.05%; H, 3.73%.

Preparation of nanoparticles

The nanoparticles (NPs) of **1** and **2** were prepared using the following method. 100 mg of **1** or **2** were added to 80 mL of anhydrous ethanol and mixed. After 12 hours, the remaining undissolved species was filtered off. 10 mL of ethanolic complex solution was added dropwise to 50 mL of cyclohexane or *n*-hexane (Tables S1 and S2) and stirred (700 rpm) for 10 minutes to produce NPs of the metal complex. The procedure was repeated with stirring for 15, 30, or 60 minutes, and the samples of the NPs so obtained are referred to as $[complex]_{Str\text{-}10}$, $[complex]_{Str\text{-}15}$, $[complex]_{Str\text{-}30}$ and $[complex]_{Str\text{-}60}$, respectively. A similar procedure was applied, using sonication instead of stirring. The corresponding

samples are referred to as $[complex]_{Son\text{-}10}$, $[complex]_{Son\text{-}15}$, $[complex]_{Son\text{-}30}$ and $[complex]_{Son\text{-}60}$.

X-ray crystallography

The X-ray diffraction data for orange needle-shaped crystals of $[Ru^{III}Cl_4(Nic)_2]^-[(CH_3)_2NH_2]^+DMF$, **1**, and yellow plate-shaped crystals of $[Ru^{III}Cl_2(3\text{-}HPA)_2]^-[3\text{-}HH_2PA]^+(EtOH)_2$, **2**, were collected at 100 K with XtaLAB Synergy-S diffractometer using CuKα radiation (λ = 1.54184 Å). The data reduction was performed in CrysAlisPro for the studied complexes, and the analytical absorption correction was applied (CrysAlis version 1.171.43.120a package of programs).[21] The compounds' structures were solved using direct methods and refined with a full-matrix least-squares procedure on F^2 (SHELX2018 program packages).[22] Table 1 summarises the data collection and refinement processes. The structural data have been deposited at the Cambridge Crystallographic Data Centre: (CCDC no. 2401926 for $[Ru^{III}Cl_4(Nic)_2]^-[(CH_3)_2NH_2]^+DMF$ and 2401927 for $[Ru^{III}Cl_2(3\text{-}HPA)_2]^-[3\text{-}HH_2PA]^+(EtOH)_2$).

The XRD analysis of the NPs of $[Ru^{III}Cl_4(Nic)_2]^-[(CH_3)_2NH_2]^+DMF$, **1**, and $[Ru^{III}Cl_2(3\text{-}HPA)_2]^-[3\text{-}HH_2PA]^+(EtOH)_2$, **2**, complexes has been examined by the PANalytical X'Pert PRO MPD diffractometer with the generator parameters 30 mA, 40 kV, Cu used as anode material and K-alpha = 1.5406 *Å*. The sample was placed on a zero-background silicon flat plate holder. The measurement was carried out in Bragg–Brentano geometry (flat plate reflection) with fixed slit sizes. A graphite crystal X-ray monochromator (oriented with the 002 plane) was used on the diffracted beam to remove Kβ radiation. The diffractograms were recorded from 0 to 60° (Fig. 1). The average crystallite size of the prepared nanoparticles was determined by using Debye Scherrer's (DS) formula, $C_s = K\lambda/\beta \cos\theta$, where C_s is the crystallite size, k is Scherer constant (0.9), λ is the XRD wavelength (1.5406 A), θ is the Bragg diffraction peak (in radian), and β is the full width at half maximum (FWHM). The crystallite size was also determined by using the Williamson–Hall plot (W–H), by plotting $\beta\cos\theta$ *versus* $4\sin\theta$ for all peaks (where β is in degrees and β is in rad) and fitting the best line gives a slope of 4ε and an intercept of $K\lambda/D$. The dislocation density and crystallite size of the prepared nanoparticles are related as $\delta = 1/D^2$, and the lattice strain is given as $\varepsilon = (\beta\cot\theta)/4$.

IR spectra were recorded with a Bruker-Optics Vertex 70v FTIR spectrometer with ATR optics (diamond crystal) in the 4000–30 cm^{-1} range.

HR-SEM was applied for the material surface imaging by using a Quanta field-emission scanning electron microscope, Quanta 3D FEG (FEI, Netherlands).

SEM/EDX was used to analyse the chemical composition of the NPs by applying a scanning electron microscope 1430 VP (LEO Electron Microscopy Ltd, England 2001) coupled with an energy dispersive X-ray spectrometer Quantax 200 with XFlash 4010 detector (Bruker AXS, Germany 2008).

DLS was used to determine the size distribution profile of nanoparticles in a suspension of 0.1 mg in 2 ml of toluene (in a quartz cuvette) mixed on the vortex (Vortex Genie 2; IKA®

Table 1 Crystal data and structure refinement parameters for $[Ru^{III}Cl_4(Nic)_2]^-[(CH_3)_2NH_2]^+DMF$, **1**, and $[Ru^{III}Cl_2(3\text{-}HPA)_2]^-[3\text{-}HH_2PA]^+(EtOH)_2$, **2**

Identification code	**1**	**2**
CCDC	2401926	2401927
Empirical formula	$C_{22}H_{26}Cl_2N_3O_{11}Ru_1$	$C_{20}H_{32}Cl_4N_5O_6Ru_1$
Formula weight. g mol^{-1}	680.43	681.37
Crystal size. mm	0.151 × 0.084 × 0.019	0.190 × 0.070 × 0.030
Crystal system	Triclinic	Monoclinic
Space group	$P\bar{1}$	$C2/c$
a. Å	8.7433(3)	32.3494(6)
b. Å	12.1709(3)	6.98030(10)
c. Å	13.4239(4)	15.8129(3)
α. °	95.958(2)	90
β. °	100.870(3)	126.725(3)
γ. °	104.916(2)	90
Volume. $Å^3$	1338.01(7)	2861.96(12)
Z	2	4
Density (calc.). g cm^{-3}	1.689	1.581
Absorption coefficient. mm^{-1}	7.151	8.242
F(000)	690	1388
Θ range. °	3.397 to 78.040	3.409 to 78.010
Reflections collected/unique	15 839/5377 [*R*(int) = 0.0412]	10 750/2914 [*R*(int) = 0.0238]
Index ranges *hkl*	$-11 \le h \le 10$, $-13 \le k \le 15$, $-16 \le l \le 16$	$-40 \le h \le 32$, $-8 \le k \le 8$, $-20 \le l \le 19$
Restraints/parameters	2/355	0/169
Goodness of fit on F^2	1.065	1.075
Final *R* indices [$I > 2\sigma(I)$]	R_1 = 0.0363, wR_2 = 0.1004	R_1 = 0.0203, wR_2 = 0.0557
R indices (all data)	R_1 = 0.0420, wR_2 = 0.1024	R_1 = 0.0210, wR_2 = 0.0560
Max electron density/e $Å^{-3}$	1.297	0.380
Min electron density/e $Å^{-3}$	−1.105	−0523

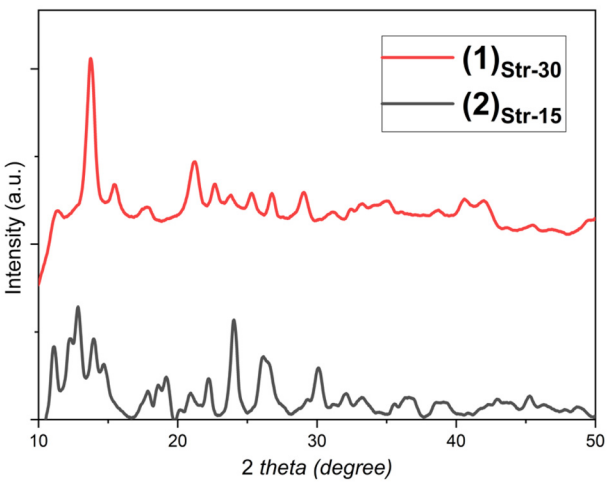

Fig. 1 X-ray powder diffraction patterns of nanoparticles of $[Ru^{III}Cl_4(Nic)_2]^-[(CH_3)_2NH_2]^+DMF_{Str\text{-}30}$ and $[Ru^{III}Cl_2(3\text{-}HPA)_2]^-$ $[3\text{-}HH_2PA]^+(EtOH)_{2Str\text{-}15}$.

Poland). Zetasizer Nano Series (Malvern Instruments, UK) was used for the measurements. Zeta potential measurements were not performed because the antisolvent used (cyclohexane) dissolves cuvettes adapted for this type of measurement.

DLS and zeta potential measurements were also performed to determine the size distribution and zeta potential of control solutions (MHB, DMEM, distilled water) and ruthenium complexes, using a Zetasizer NanoSeries (Malvern Instruments, Malvern, UK). Measurements were performed immediately after the addition of ruthenium complexes to bacterial growth medium (MHB), cell culture medium (DMEM), or distilled water, and again after 24 hours (for MHB and distilled water) or 48 hours (for DMEM) of incubation at 37 °C. The final concentrations of ruthenium complexes and the incubation times precisely mirrored the conditions employed in the biological assays. Dynamic Light Scattering (DLS) was utilised to analyse the size distribution. The zeta potential (ζ) was calculated based on the Smoluchowski equation. All measurements were carried out in triplicate for each sample. UV cuvettes were used for size determination, while folded capillary cells were employed for zeta potential measurements.

EPR experiments were performed using a Bruker Elexsys E500 spectrometer operating at 9.6 (X-band) frequency. The spectrometer was equipped with an NMR teslameter (ER 036TM) and a frequency counter (HP 5342 A). Spectra were recorded at 77 K for solutions (10 mg in 1 ml of methanol/ethylene glycol mixture, volume ratio 2 : 1) at 77 K (X-band). The modulation field amplitude and frequency were set to 10.0 mT and 100 kHz, respectively. Microwave power was maintained at 20 mW. All simulations of EPR spectra were carried out using EasySpin 6.[23,24] Resonator backgrounds were carefully subtracted from the spectra.

DFT calculations were performed using the ORCA 5 suite of programs.[25–27] Scalar relativistic effects were accounted for using the zeroth-order regular approximation (ZORA) with the model potential approximation proposed by van Wüllen.[28] The SARC-ZORA-TZVP basis set was employed for ruthenium, while the ZORA-def2-TZVP basis set (def2-TZVP re-contracted for ZORA by D. A. Pantazis) was used for all remaining atoms.[29–31] The resolution of identity (RI) approximation was applied[32,33] with the corresponding auxiliary basis sets[30,34] to enhance computational efficiency. The structures of the $[Ru^{III}Cl_4(Nic)_2]^-$ and $[Ru^{III}Cl_2(3\text{-}HPA)_2]^-$ anions for the calculations were taken from X-ray diffraction experiments, but all hydrogen atom positions were optimised using the TPSS functional.[35] *g* Tensor calculations at the DFT level were carried out using the coupled perturbed approach[36,37] with hybrid and *meta*-hybrid functionals: PBE0,[38] Becke's half-and-half functional (BHandHLYP),[39] TPSSh[35] and TPSS0.[40,41] The PBE0 and TPSS0 functionals were also tested, and the Hartree–Fock exchange increased to 50% (labelled PBE0-50 and TPSS0-50, respectively). All calculations employed an accurate integration grid (DefGrid2) and tight SCF convergence criteria (TightSCF). All visualisations were done using Gabedit.[42]

Cell culture. Hepatocellular carcinoma Hep-G2 cells were obtained from the European Collection of Authenticated Cell Cultures (Sigma Aldrich). L929 murine fibroblast cells and human epithelial colorectal adenocarcinoma Caco-2 cells were purchased from the American Type Culture Collection. All cell lines were cultured at 37 °C in 5% CO_2 and 95% humidity in Dulbecco's modified Eagle's medium (DMEM High Glucose; Biowest) supplemented with 10% fetal bovine serum (Biological Industries) and 1% penicillin/streptomycin (Capricorn Scientific GmbH). Cells were passaged upon reaching approximately 70% confluence using 0.05% trypsin–EDTA solution (Capricorn Scientific GmbH).

Cell viability. The cytotoxic effects of ruthenium complexes $[Ru^{III}Cl_4(Nic)_2]^-[(CH_3)_2NH_2]^+$DMF, **1**, and $[Ru^{III}Cl_2(3\text{-}HPA)_2]^-[3\text{-}HH_2PA]^+(EtOH)_2$, **2**, on cells were assessed using the MTT (3-(4,5-dimethylthiazolyl)-2,5-diphenyl-tetrazolium bromide; Thermo Fisher Scientific) assay. Briefly, 5×10^3 L929 fibroblasts, 5×10^3 Hep-G2, 4×10^3 Caco-2 cells were seeded into 96-well plates (Jet Biofil) in 100 µl supplemented DMEM and pre-incubated for 24 h at 37 °C. Then, cells were treated with ruthenium complexes at concentrations of 0.025, 0.05, 0.1, and 0.5 mg ml^{-1}, prepared in DMSO and filtered through 0.22 µm polyamide filters. Equal volumes of DMSO were added to control wells. After 48 h incubation, the medium was removed, and 100 µl of MTT solution (0.5 mg ml^{-1}) was added to each well. Plates were incubated for three hours at 37 °C. After aspirating the MTT solution, 50 µl of DMSO (100% v/v) was added to dissolve the resulting formazan crystals. Absorbance was measured at 570 nm with a reference at 630 nm using a Varioscan™ LUX Multimode Microplate Reader. Cell viability was expressed as a percentage relative to untreated controls. Each experiment was performed in five independent replicates. Cell morphology and confluence after 48 hours of treatment were assessed using an inverted phase-contrast microscope (Olympus EP50). Data are presented as mean ± SEM. Statistical significance was evaluated using one-way ANOVA followed by Tukey's *post-hoc* test, performed with GraphPad Prism version 8.0.2 (La Jolla, CA, USA). The significance was indicated as follows: * $p < 0.05$; ** $p < 0.01$; *** $p < 0.001$. For data where cell viability values exceeded the control, the '#' symbol was used instead of '*' to indicate statistical significance.

Determination of the minimum inhibitory concentration (MIC). The antibacterial studies were performed using the broth microdilution method. The complex **1** or **2** solution was prepared in DMSO, so the concentration was 10 mg ml^{-1}. This solution was filtered through a polyamide filter with pores of 0.22 µm. Then, a series of dilutions was prepared by successive two-fold dilutions with DMSO filtered through a 0.22 µm filter. The concentrations of the complex solutions used in the study were equal to 10 mg ml^{-1}, 5 mg ml^{-1}, 2.5 mg ml^{-1}, 1.25 mg ml^{-1} and 0.625 mg ml^{-1}. The study used a 100-fold diluted 0.5 McFarland bacterial suspension (bacterial working suspension), prepared in sterile Muller-Hinton Broth (MHB) from 24 h bacterial cultures. 190 µl of bacterial working suspension was added to separate wells of a sterile 96-well plate with a U-shape bottom and supplemented with 10 µl of the tested complex solutions. Thus, the final concentrations of the

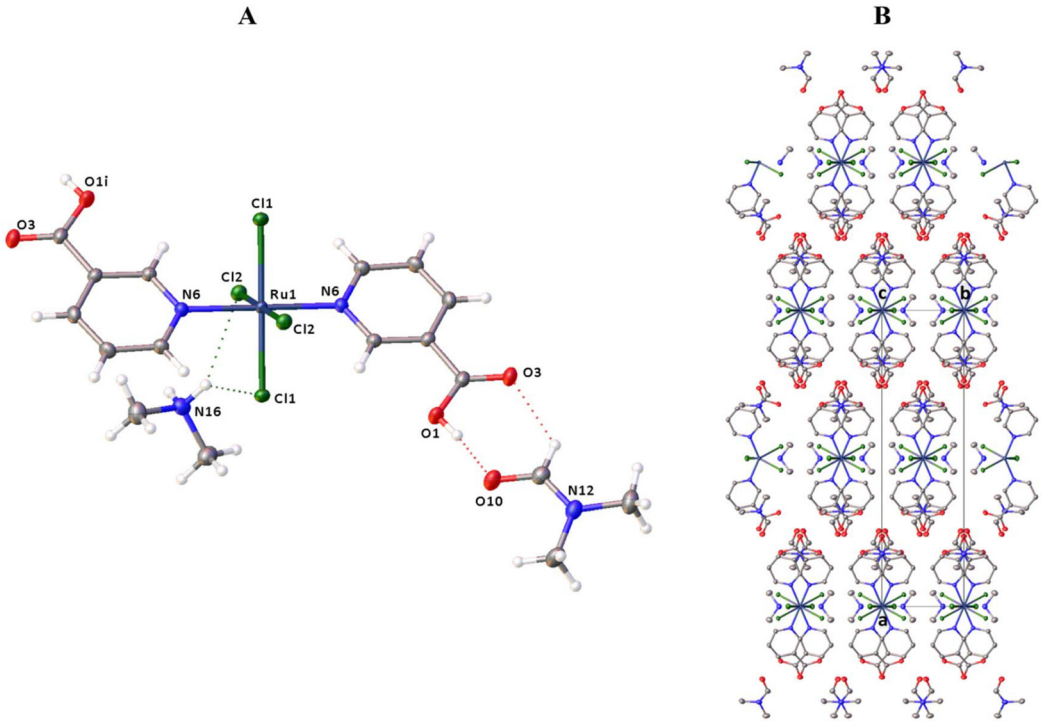

Fig. 2 (A) The structure of $[Ru^{III}Cl_4(Nic)_2]^-[(CH_3)_2NH_2]^+$DMF (the thermal ellipsoids plotted at 30% probability) shows intermolecular hydrogen bonding interactions (dashed line). (B) Crystal packing along the *c*-axis. The hydrogen atoms were omitted for clarity.

studied complexes were 0.5 mg ml^{-1}, 0.25 mg ml^{-1}, 0.125 mg ml^{-1}, 0.0625 mg ml^{-1}, and 0.0312 mg ml^{-1}. The positive control contained a bacterial suspension and was supplemented with 10 µl of sterile DMSO (0 mg ml^{-1} of complex solution). For the negative control, a sterile medium was used instead of a bacterial suspension while maintaining the concentration of the complex for each of the variants of the final concentration. The plates were incubated overnight at 37 °C. The viability of bacteria was assessed using a 100 µg ml^{-1} resazurin sodium salt solution. 12 µl of the prepared solution was added to each plate well. The plates were incubated at 37 °C for 1 hour. Detection was performed based on fluorescence measurements (E_{ex} = 560 nm, E_{em} = 590 nm) using a microplate reader (VarioskanLux, ThermoFisherScientific Oy, Vantaa, Finland). The fluorescence was calculated by subtracting the negative control from the tested values. The reduction in bacterial viability was calculated as a percentage of normal viability, where the positive control was assumed to be 100%. The analysis was performed in triplicate for each tested concentration. In the study, we use three Gram-negative *Klebsiella pneumoniae* strains, namely ATCC BAA-1705 strain (carbapenemase-producing, with KPC gene), ATCC 10031 (drug-sensitive), and the B34 strain from the deposit of ICNT NCU in Toruń, isolated from a diabetic foot. Moreover, three Gram-positive *Staphylococcus aureus* strains were used: ATCC BAA-1026 (MRSA), ATCC 29213 (drug-sensitive), and strain B5 from the deposit of ICNT NCU in Toruń, isolated from a diabetic foot.[43]

Results & discussion

X-ray structure of $[Ru^{III}Cl_4(Nic)_2]^-[(CH_3)_2NH_2]^+$DMF

The complex $[Ru^{III}Cl_4(Nic)_2]^-[(CH_3)_2NH_2]^+$DMF (Fig. 2) crystallises in a monoclinic *C*2/*c* space group with a Ru(III) ion positioned at the inversion centre. The bond lengths and angle values in the ruthenium coordination sphere are in the range of 2.0896(12)–2.3542(3) Å and 88.80(4)–180.0°, respectively (Table S3). The coordination sphere of Ru(III) adopts a distorted octahedral geometry and is composed of four chloride atoms and two nitrogen atoms coming from two *nic* ligands. The asymmetric part contains half of the ruthenium complex anion, half of the $[(CH_3)_2NH_2]^+$ cation, and a DMF molecule. Dimethylamine participates in N–H···Cl and C–H···Cl-type interactions, while C–H stabilises the DMF molecule···O and O–H···O type interactions (Table S4). The analysis of the $[Ru^{III}Cl_4(Nic)_2]^-[(CH_3)_2NH_2]^+$DMF structure also revealed C15–H15B···$\pi_{(C4\cdots C9)}$[1 − *x*, 1 − *y*, 1 − *z*], with distance C···π being 3.694(2) Å.

X-ray structure of $[Ru^{III}Cl_2(3\text{-HPA})_2]^-[3\text{-}HH_2PA]^+(EtOH)_2$

The compound $[Ru^{III}Cl_2(3\text{-HPA})_2]^-[3\text{-}HH_2PA]^+(EtOH)_2$ crystallises in the triclinic $P\bar{1}$ space group with anion $[Ru^{III}Cl_2(3\text{-HPA})_2]^-$, cation $[3\text{-}HH_2PA]^+$ and two molecules of ethanol in the asymmetric unit (Fig. 3). The Ru(III) atom has a distorted octahedral geometry consisting of two chloride ions, N and O atoms of two 3-HPA ligands. The bond lengths in the ruthenium coordination sphere are in the range of 2.035(2)–2.3382

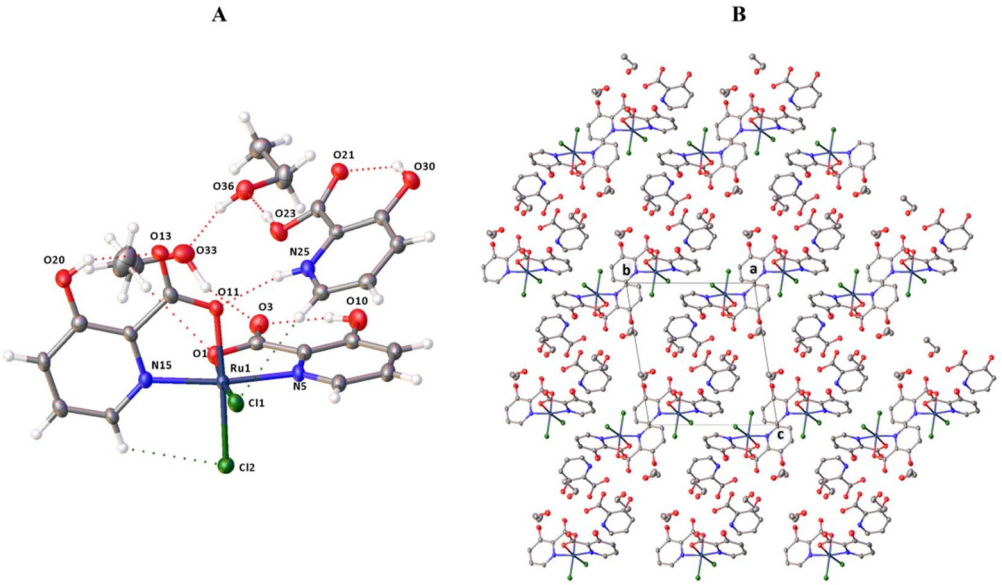

Fig. 3 (A) The structure of $[Ru^{III}Cl_2(3\text{-}HPA)_2]^-[3\text{-}HH_2PA]^+(EtOH)_2$ (the thermal ellipsoids plotted at 30% probability) with intermolecular hydrogen bonding interactions (dashed line). (B) Crystal packing along the *a*-axis. The hydrogen atoms were omitted for clarity.

(7) Å, and the angles are in the range of 80.94(9)–177.07(6) ° (Table S3).

The $[3\text{-}HH_2PA]^+$ (cation participates in intra- and intermolecular hydrogen bonds of the O–H···O and N–H···O type) (Table S4). Meanwhile, the solvent molecules (EtOH) interact with each other as well as with the cation $[3\text{-}HH_2PA]^+$ and complex anion $[Ru^{III}Cl_2(3\text{-}HPA)_2]^-$ (Table S4). Analysis of the crystal packing also revealed the presence of π···π interactions. Interactions between 6-membered rings of ligands coordinated with the Ru(III) ion have been observed. These are $\pi_{(C4\cdots C9)}\cdots\pi_{(C4\cdots C9)}[-x, 1-y, -z]$ interactions with a distance of 3.7228(16) Å and $\pi_{(C14\cdots C19)}\cdots\pi_{(C14\cdots C19)}[1-x, -y, -z]$ interactions with a distance of 3.6553(18) Å.

Microscopic studies

The SEM technique was utilised to study the morphology of the two complexes (Fig. S1). Samples prepared on a silicon plate reveal the complex morphology of irregular, radiating plates or flakes. The elemental compositions of the two complexes $[Ru^{III}Cl_4(Nic)_2]^-[(CH_3)_2NH_2]^+DMF$, **1**, and $[Ru^{III}Cl_2(3\text{-}HPA)_2]^-[3\text{-}HH_2PA]^+(EtOH)_2$, **2**, were identified by EDX analyses of samples taken from different batches of the products. As presented in Fig. S1, typical EDX spectra of the obtained salts exhibit C, N, O, Cl, and Ru peaks, characteristic of the component elements of the **1** and **2** complexes. The lack of signals corresponding to elements other than expected indicates the purity of the obtained samples. Aluminium detected in the analyses originates from the microscope table.[44]

Spectroscopic studies

The infrared spectra of the complexes **1** and **2** are given in Fig. S2. At frequencies around 3073 and 3097 cm^{-1}, O–H stretching vibrations of the carboxyl group appear. C–H stretching vibrations from the aromatic ring are seen in the range of around 2939–2800 cm^{-1}. C=O stretching vibrations for the uncoordinated carboxyl group occur at a wavelength of around 1747–1709 cm^{-1}. At about 1630 cm^{-1}, symmetric and asymmetric C=C stretching vibrations of the aromatic ring are observed. For the ν(C–C) and ν(C=N) vibrations, bands appear in the range of 1590–1450 cm^{-1}, while at 1650–1500 cm^{-1}, deformation vibrations for N–H. C–O stretching vibrations occur in the range of 1430–1100 cm^{-1}. Sharp bands of high or medium intensity at 1286, 1245, 1050, 850–845, 753, 695, and 480 cm^{-1} are characteristic of vibrations originating from coordinated nicotinic acid (Fig. S2a). The bands in the 890–860 cm^{-1} and 790–810 cm^{-1} range are typical for the 3-hydroxypicolinate ligand (Fig. S2b). Typical vibrations for the pyridine ring occur at about 850–820 cm^{-1} and around 1600 cm^{-1}. At frequencies around 420 cm^{-1}, a band assigned to the ν(Ru–N) vibrations appears. Two bands in the far infrared range (280–250 cm^{-1}) correspond to Ru–Cl's symmetric and asymmetric stretching vibrations.[44,45]

The EPR spectra of **1** ($[Ru^{III}Cl_4(Nic)_2]^-[(CH_3)_2NH_2]^+DMF$) and **2** ($[Ru^{III}Cl_2(3\text{-}HPA)_2]^-[3\text{-}HH_2PA]^+(EtOH)_2$) in methanol/ethylene glycol (2 : 1) mixtures are shown in Fig. 4. Both spectra are characteristic of an $S = 1/2$ system and do not exhibit hyperfine structure from ^{99}Ru ($I = 5/2$, 12.76%) or ^{101}Ru ($I = 5/2$, 17.06%). Therefore, the spin Hamiltonian for the low-spin Ru(III) centres (d^5, $S = 1/2$) can be given as: $\hat{H}_S = \mu_e(B_x g_x \hat{S}_x + B_y g_y \hat{S}_y + B_z g_z \hat{S}_z)$.

Complexes **1** and **2** exhibit slightly rhombic EPR signals ($g_x > g_y \gg g_z$), with the perpendicular components of the *g* tensor (g_x and g_y) being more clearly resolved for **2**. In contrast, for **1**, significant line broadening due to *g* strain makes the parallel component (g_z) challenging to observe without careful subtraction of the resonator background.[46] Similar broadening

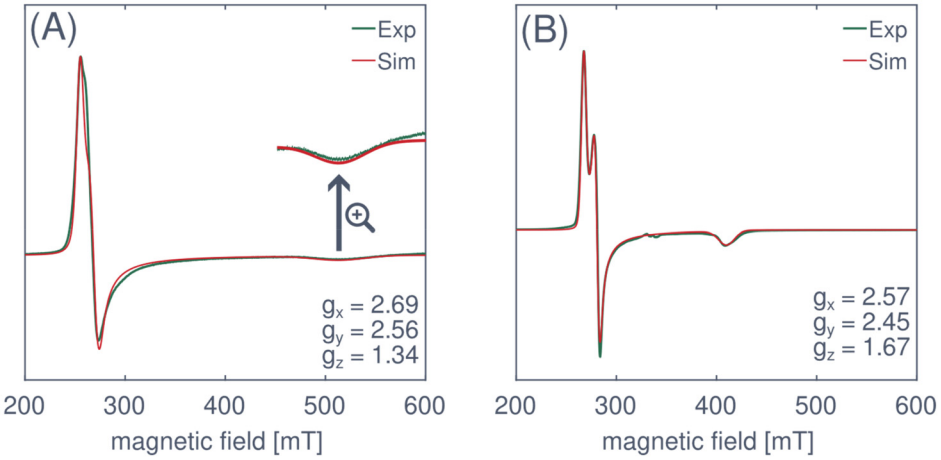

Fig. 4 EPR spectra of complex **1** (panel A) and complex **2** (panel B).

effects have been previously reported for Ru(III) complexes.[47,48] They are observed to some extent for the g_x and g_y lines, rendering them less fully resolved in **1** compared to **2**.

The principal g components for **1** and **2** are characteristic of low-spin Ru(III).[44,47–52] However, g_x and g_y are noticeably higher for **1**, while g_z is lower, reflecting differences in their coordination environments. Complex **1** features four chloride ligands in the equatorial plane, whereas **2** has two oxygens and two chlorides, leading to distinct electronic properties, especially changes in the energy of $(t_{2g})^5$ orbitals.[46,50,53]

To gain insight into the energies and electronic characteristics of the d orbitals using experimental EPR data, we employed the method developed by McGarvey,[53,54] which has been found successful for various d^5 systems,[49,51,53,55,56] including Ru(II)–Ru(III) ion pairs.[44,57] By solving the McGarvey equations, we found that, for **1** and **2**, the d_{xy} orbital lies above d_{xz} and d_{yz}. Consequently, the electronic configuration of Ru(III) in **1** and **2** is $(d_{xz})^2(d_{yz})^2(d_{xy})^1$. Moreover, both complexes' excited states are well separated from the ground state, resulting in negligible mixing of the lowest Kramers doublet with higher-energy states. Details of this procedure are given in the SI.

DFT calculations

We performed DFT calculations to confirm that the unpaired electron in **1** and **2** occupy the d_{xy} orbital. The predicted d-orbital splitting for both complexes is shown in Fig. 5A, along with the respective orbital isosurfaces. Our computational results confirm that the singly occupied molecular orbitals (SOMOs) have a dominant contribution from the d_{xy} atomic orbitals of ruthenium. Unlike orbitals with d_{xz}, d_{yz} or $d_{x^2-y^2}$ characters, the SOMOs exhibit limited antibonding interactions with the ligands, suggesting that spin density delocalisation onto the ligands should be relatively small in **1** and **2**. Although spin density isosurfaces (Fig. 5B) reveal some transfer of the unpaired electron to donor atoms, Löwdin spin population analysis at the BHandHLYP level confirms that 91.3% and 90.7% of the unpaired electron density remains localised on the Ru(III) centre in **1** and **2**, respectively.

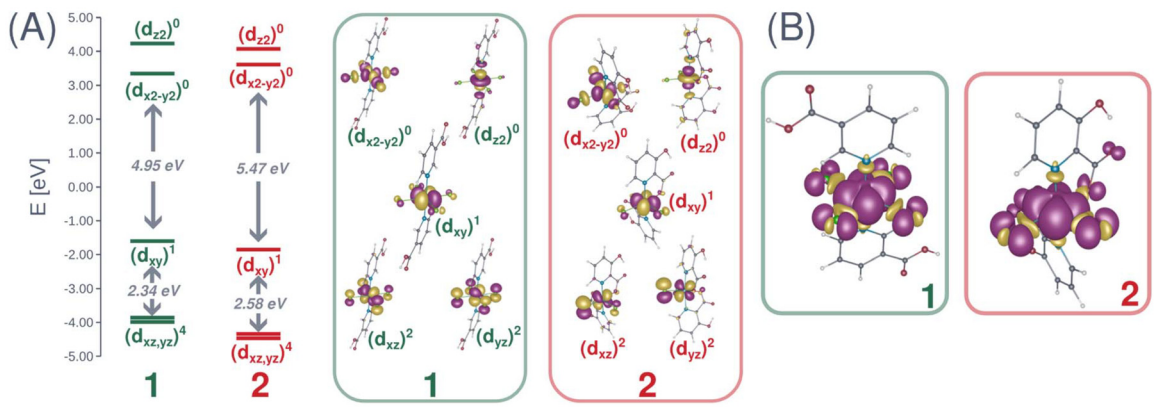

Fig. 5 Results of DFT calculations using the hybrid functional BHandHLYP for complexes **1** and **2**: splitting of the quasi-restricted orbitals and their isosurfaces contoured at 0.05 a.u. (panel A) and spin density isosurfaces contoured at 0.001 a.u., with purple representing positive (α-type) and yellow representing negative (β-type) spin densities (panel B).

We also used DFT to calculate the principal components of the *g* tensor for **1** and **2**. Although some quantitative discrepancies were observed, the *g* values obtained from DFT calculations qualitatively aligned well with EPR experimental data and accurately reproduced the *g* tensor pattern found for **1** and **2** (Table S6). Consequently, the electronic structures derived from these theoretical calculations, summarised in Fig. 5, provide a reliable model for **1** and **2**.

Nanoparticles of $[Ru^{III}Cl_4(Nic)_2]^-[(CH_3)_2NH_2]^+$ (NPs(1)) and $[Ru^{III}Cl_2(3\text{-}HPA)_2]^-[3\text{-}HH_2PA]^+$ (NPs(2))

Applying the anti-solvent method combined with magnetic stirring or sonication led to the nano/submicron particle formation of complexes. Fig. 6, 7, and S3–S6 present high-resolution scanning electron (HR-SEM) images and dynamic light scattering (DLS) size distribution profiles of the ellipsoidal, round and somewhat polygonal, primarily rectangular particles of **NPs(1)** and **NPs(2)**, formed under various experimental conditions. A close look at the SEM images reveals similar shapes of the given complex particles obtained by applying magnetic stirring. In contrast, sonication produces particles with a variety of less regular shapes. Furthermore, a broad range of particle sizes (*ca.* 37–372 nm for **NPs(1)** and 53–263 nm for **NPs(2)**) can be accounted for in terms of aggregation during reaction suspension filtration and drying of the solid material.

DLS data collected for the examined particles (Fig. 6, 7, and S3–S6) demonstrate irregular time-dependent size fluctuation, *i.e. ca.* 92–282 nm for $[Ru^{III}Cl_4(Nic)_2]^-[(CH_3)_2NH_2]^+$ and 180–255 nm for $[Ru^{III}Cl_2(3\text{-}HPA)_2]^-[3\text{-}HH_2PA]^+$. Nevertheless, the smallest particles of both complexes were found in samples stirred or sonicated for 10 minutes during the syntheses. The larger particle sizes measured by DLS than those estimated from SEM images are unsurprising. One should remember that DLS and SEM approaches are complementary techniques that provide insights into nanoparticle size distribution and morphology. Yet, they fundamentally differ in the measurement process. DLS measures the hydrodynamic dia-

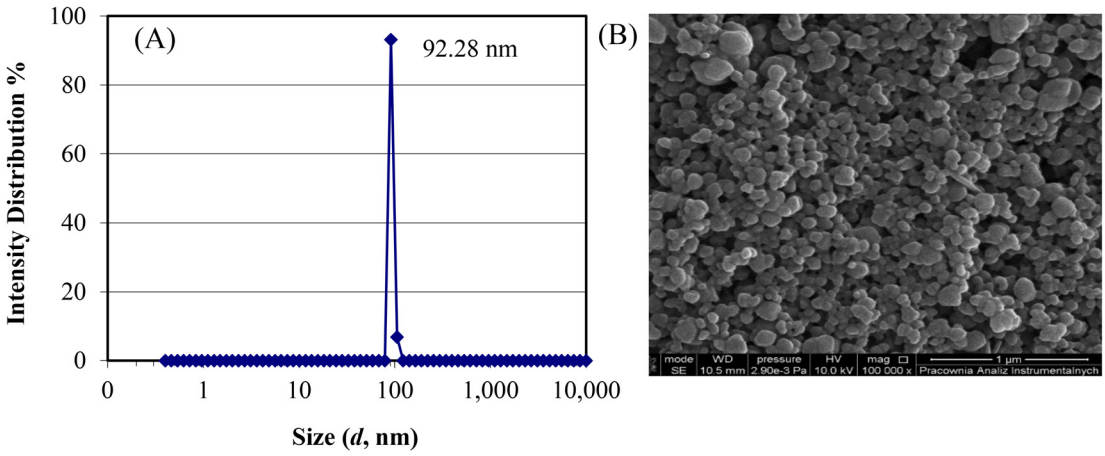

Fig. 6 Hydrodynamic size (A) and SEM image for NPs (B) of $[Ru^{III}Cl_4(Nic)_2]^-[(CH_3)_2NH_2]^+DMF_{Str\text{-}10}$ obtained from the anti-solvent method.

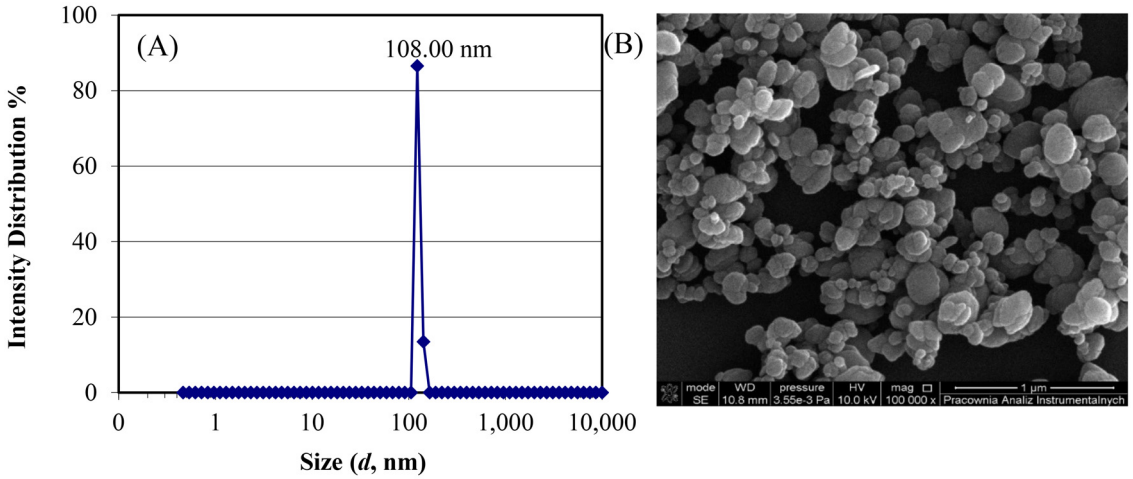

Fig. 7 Hydrodynamic size (A) and SEM image for NPs (B) of $[Ru^{III}Cl_4(Nic)_2]^-[(CH_3)_2NH_2]^+DMF_{Son\text{-}10}$ obtained from the anti-solvent method.

meter of colloidal particles in suspension, including the core particle size, the solvation shell, and any associated dynamic layers (*e.g.* hydration shells, polymer coatings, or loosely bound counterions).

In contrast, SEM provides direct visualisation of particle morphology after solvent evaporation, eliminating the solvation shell and surface-bound species that potentially alter particles' spatial arrangement due to capillary forces during drying.[58] The present study interpreted the DLS measurements within the Smoluchowski approximation, which describes Brownian motion and light scattering in colloidal dispersions (Fig. S3–S6). According to this framework, the intensity-weighted hydrodynamic diameter derived from DLS corresponds to an effective radius that accounts for the dynamic interactions between the solvated nanoparticle and its surrounding medium. It is particularly relevant for systems involving ionic or polar ligands, such as the ruthenium(III) complexes examined here, where the solvation shell significantly influences the observed particle size. The observed discrepancies between DLS and SEM data stem from these fundamental differences in measurement principles. While DLS characterises nanoparticles in a fully solvated state, reflecting their behaviour in biological or catalytic environments, SEM measures the dried-state dimensions, where capillary forces may induce particle aggregation, deformation, or shrinkage. The size distributions obtained from DLS suggest that the studied systems exist as stable colloidal suspensions with a polydispersity index (PDI) indicative of moderate heterogeneity. The Smoluchowski approximation further supports the notion that nanoparticle motion in the dispersions follows the diffusive behaviour expected for colloidal systems, confirming their stability under the chosen experimental conditions.[59] In particular, the hydrodynamic diameters obtained for $[Ru^{III}Cl_4(Nic)_2]^-[(CH_3)_2NH_2]^+$DMF and $[Ru^{III}Cl_2(3\text{-}HPA)_2]^-[3\text{-}HH_2PA]^+(EtOH)_2$ exhibit a broad distribution, likely due to variations in solvation layer thickness and the presence of small aggregates. While providing high-resolution structural insights, the SEM analysis captures only the dehydrated particle morphology and does not account for solvent-mediated interparticle interactions. As such, the combination of DLS and SEM enables a more comprehensive understanding of the physicochemical properties of these ruthenium-based systems, bridging their behaviour in solution and the solid state. The consistency of the DLS results with Smoluchowski's approximation supports the interpretation that these complexes exist in colloidal form rather than as discrete molecular species in solution.

The obtained NPs of both complexes under selected conditions were also investigated using X-ray powder diffraction (Fig. 1). The collected data were processed using the Scherrer and Williamson–Hall methods (Fig. S7), and the values of the crystallite sizes, D, and elastic strain are given in Table S5. The crystallite sizes of 15 and 8.92 nm obtained for **NPs(1)**$_{Str\text{-}30}$ and **NPs(2)**$_{Str\text{-}15}$, respectively, from the Williamson–Hall (W–H) plot, are smaller than those of 18 and 24.22 nm for **NPs(1)**$_{Str\text{-}30}$ and **NPs(2)**$_{Str\text{-}15}$, respectively, calculated using the Scherrer equation. This discrepancy arises because the W–H method accounts for crystallite size and lattice strain, whereas the Scherrer equation considers only size broadening. However, this computation (W–H) is statistically more suitable than merely averaging individual values. The presence of significant compressive strain (1.3%) and high dislocation density (12.57×10^{12} lines per m^2) in **NPs(2)**$_{Str\text{-}15}$ mainly contributes to additional peak broadening, leading to a smaller crystallite size estimation in the W–H analysis. The X-ray determined average crystallite size of **NPs(1)**$_{Str\text{-}30}$ and **NPs(2)**$_{Str\text{-}15}$ agrees nicely with the particle size of the same sample obtained by other methods (see Table 1), which therefore demonstrates the nanoscale of the examined complex.

Hydrodynamic size and zeta potential of ruthenium(III) complexes in aqueous and biological media: DLS investigation

In this study, we systematically investigated the electrokinetic properties of ruthenium(III) complex particles in aqueous and biologically relevant media – Mueller–Hinton Broth (MHB) and Dulbecco's Modified Eagle's medium (DMEM). Dynamic light scattering (DLS) measurements were employed to determine the hydrodynamic radii and particle-size distributions of the colloidal suspensions. Zeta-potential analyses quantified their surface charge and colloidal stability. This physicochemical characterisation is crucial for interpreting the complexes' bioavailability and biological activity *in vitro* and *in vivo* since hydrodynamic size and surface charge strongly influence aggregation behaviour and interactions with biological systems.

Fig. S8 presents particle size distribution plots for both ruthenium complexes and the aqueous solutions used for cell culture, showing data acquired before and after incubation at 37 °C. The ruthenium complexes analysed did not form real solutions, but appeared as dispersive systems containing one or more populations of aggregates. Their behaviour showed considerable variability, depending on the environment and concentration.

In aqueous solutions (Fig. S8a, S8a* and S8a′), control solutions, *i.e.* distilled water (sample A) and water with 5% DMSO (sample B), particle sizes ranged between 344.5–368.3 nm. The zeta potential in sample B was −17.3 mV, increasing to −29 mV after 24 hours of incubation, suggesting improved colloidal stability. Ruthenium complexes at higher concentrations (0.5 mg ml^{-1}; samples C and E) formed aggregates between 200–400 nm with a zeta potential near zero (*e.g.* +1.89 mV for sample C after 24 h), indicating low electrostatic stability and aggregation tendency (DLVO theory). At lower concentrations (0.0312 mg ml^{-1}; samples D and F), bimodal distributions appeared, and zeta potential values remained low (−3 to −5 mV), suggesting aggregation governed by van der Waals forces rather than electrostatic repulsion. According to DLVO theory, such zeta potential values confirm that in water, the system's stability is not due to electrostatic repulsion, and possible stabilisation may be related to other mechanisms, such as steric stabilisation.

Studies in MHB medium (Fig. S8b, S8b* and S8b′) allowed us to evaluate the electrokinetic behaviour under conditions simulating the microbiological environment. In MHB, even control samples showed a tendency to component aggregation (low dispersion stability). The zeta potential was more negative (−13 to −29 mV), implying increased electrostatic stability. However, complex aggregation in MHB was highly variable. The aggregation of ruthenium complexes in MHB strongly depended on complex concentration and structure. For example, after 24 hours, $[Ru^{III}Cl_2(3\text{-}HPA)_2]^-[3\text{-}HH_2PA]^+(EtOH)_2$, **2** at 0.5 mg ml^{-1} formed a dominant 64 nm population alongside substantial aggregates (~4804 nm), while maintaining a relatively high zeta potential (−20 mV). Significant aggregation occurred at 0.0312 mg ml^{-1} despite increasing zeta potential, suggesting other aggregation mechanisms, such as hydrophobic interactions or interactions with medium proteins and for the $[Ru^{III}Cl_4(Nic)_2]^-[(CH_3)_2NH_2]^+DMF$, **1**, complex large aggregates formed at lower concentrations even with high zeta potentials, indicating the dominance of strong attractive forces beyond the classical DLVO model.

In DMEM medium (Fig. S8c, S8c* and S8c′), all samples exhibited trimodal particle size distributions, including small (11–63 nm) and larger (700–2600 nm) aggregates from the medium itself. The introduction of ruthenium(III) complexes affected the colloidal structure of the systems. For the $[Ru^{III}Cl_2(3\text{-}HPA)_2]^-[3\text{-}HH_2PA]^+(EtOH)_2$ complex, **2**, at 0.5 mg ml^{-1} (sample C), 26.5 nm particles initially dominated (63%), but after 48 h, even smaller particles (21.7 nm, 84%) prevailed, alongside a new ~1.8 μm fraction. A similar trend was observed at a lower concentration (sample D), with 28 nm particles reaching 98% intensity after incubation. In $[Ru^{III}Cl_4(Nic)_2]^-[(CH_3)_2NH_2]^+DMF$, **1**, complex (E, F), small particles (~19–24 nm) dominated after 48 h. However, larger aggregates (>3 μm) emerged in sample F. All samples containing ruthenium(III) complexes exhibited a negative zeta potential ranging from −6.4 to −9.2 mV, indicating limited colloidal stability and favouring aggregate formation, especially at higher concentrations and longer incubation times.

The results of DLS and zeta potential measurements show that both $[Ru^{III}Cl_2(3\text{-}HPA)_2]^-[3\text{-}HH_2PA]^+(EtOH)_2$ **2**, and $[Ru^{III}Cl_4(Nic)_2]^-[(CH_3)_2NH_2]^+DMF$, **1**, form dispersive systems composed of particles that tend to aggregate in different ways depending on the surrounding medium and concentration. Low zeta potential values in water and DMEM indicate poor electrostatic stabilisation, favouring aggregation, as predicted by DLVO theory. In contrast, in MHB medium, the zeta potential was generally more negative, which suggests improved electrostatic stabilisation. However, even in MHB, aggregation still occurred, indicating that other factors, such as steric effects, hydrophobic interactions, or interactions with proteins, influence particle behaviour. Notably, the extent and type of aggregation differed between the two complexes, especially at lower concentrations, which could affect their availability and activity in biological systems. Therefore, thorough physicochemical characterisation of these systems in biologically relevant environments is crucial to better understand and interpret their biological effects.

Ruthenium complexes: cytotoxicity and morphological effects on cell lines

The viability of L929 fibroblasts, Hep-G2 and Caco-2 cells after treatment with $[Ru^{III}Cl_4(Nic)_2]^-[(CH_3)_2NH_2]^+DMF$, **1**, and $[Ru^{III}Cl_2(3\text{-}HPA)_2]^-[3\text{-}HH_2PA]^+(EtOH)_2$, **2**, complexes at four different concentrations: 0.025, 0.05, 0.1 and 0.5 mg ml^{-1} was assessed using the MTT assay. The results showed that $[Ru^{III}Cl_2(3\text{-}HPA)_2]^-[3\text{-}HH_2PA]^+(EtOH)_2$ complex, **2**, at all concentrations tested, exhibited a cytotoxic effect on the mentioned three cell lines – L929 fibroblasts, Caco-2 and Hep-G2 after 48 h incubation.

Cell viability decreased with increasing complex concentration (Fig. 8a and b), reaching less than 23%, 52%, 34% at 0.1 mg ml^{-1} for L929, Hep-G2 and Caco-2 cells, respectively. Toxicity against L929 fibroblast cells suggests that the complex does not distinguish between healthy and cancerous cells, which may limit its therapeutic utility. It is likely to have non-selective and systemic toxicity, limiting its potential as a direct

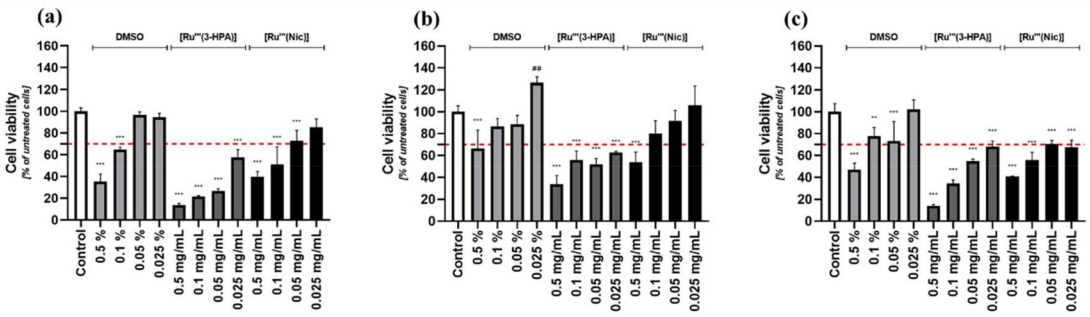

Fig. 8 Cell viability of L929 fibroblasts (a), Hep-G2 cells (b), and Caco-2 cells (c) cultured on the control with DMSO, $[Ru^{III}Cl_2(3\text{-}HPA)_2]^-[3\text{-}HH_2PA]^+(EtOH)_2$ and $[Ru^{III}Cl_4(Nic)_2]^-[(CH_3)_2NH_2]^+DMF$ samples compared with the non-treated cells in control wells (100%) for 48 h. Data are shown as mean standard error of the mean (SEM) of five independent experiments. The significance was indicated as follows: ** $p < 0.01$; *** $p < 0.001$. Pound signs denote differences between the cells cultured on the control with DMSO (## $p < 0.01$). The limit of cytotoxicity was marked with a dashed horizontal line.

anti-tumour drug, but could still be developed with targeting or structural modifications. In addition, it should be noted that DMSO, used as a solvent to dilute ruthenium complexes, can affect cytotoxicity results. Even if the complex is not highly toxic, the presence of DMSO may exacerbate the effect by facilitating transport into the cell.[60,61] Our studies have shown that DMSO at concentrations ≥0.1% is toxic to L929 mouse fibroblast cells. Application of DMSO at concentrations ≤0.1% is nontoxic to Caco-2 and Hep-G2 cells; however, the number of cells (at 0.1 and 0.05% DMSO concentration) is reduced relative to the untreated DMSO control. DMSO in the ruthenium complex can affect toxicity by, for example, increasing membrane permeability, which affects the uptake of compounds (*e.g.*, ruthenium complexes).[61,62] An effective way to eliminate this problem could be to bind the $[Ru^{III}Cl_2(3\text{-}HPA)_2]^-[3\text{-}HH_2PA]^+(EtOH)_2$ complex, **2**, to a biological carrier (*e.g.* protein, peptide, liposome, polymer or nanocarrier); this should also affect the potential increase in selectivity against cancer cells.[63–66] Replacing DMSO with another carrier eliminates the problem of its toxicity. In addition, the carrier can also protect metal complexes that are unstable in aqueous solutions from hydrolysis or ligand exchange.[67,68] We obtained different results for the other ruthenium complex analysed – $[Ru^{III}Cl_4(Nic)_2]^-[(CH_3)_2NH_2]^+$DMF, **1**. The highest viability of L929 cells (~85%) was observed at 0.025 mg ml^{-1}, indicating low toxicity at this dose (Fig. 8a). The concentration of the Nic complex at 0.05 mg ml^{-1} is at the limit of its cytotoxicity (~73%) compared to the control sample (100%). Cell viability decreased with increasing $[Ru^{III}Cl_4(Nic)_2]^-[(CH_3)_2NH_2]^+$DMF complex, **1**, concentration (Fig. 8), reaching less than 51%, 80%, 56% at 0.1 mg ml^{-1} for L929, Hep-G2 and Caco-2 cells, respectively, after 48 h incubation. Moreover, this complex was found to be nontoxic to hepatocellular carcinoma (Hep-G2) at concentrations above 0.1 mg ml^{-1} (Fig. 8b). Importantly, the complex above is toxic at all concentrations tested against human epithelial colorectal adenocarcinoma (Caco-2) (Fig. 8c). Therefore, the $[Ru^{III}Cl_4(Nic)_2]^-[(CH_3)_2NH_2]^+$DMF complex, **1**, may have a selective cytotoxic effect, acting mainly on cells of intestinal origin, which may be beneficial, for example, in the treatment of colorectal cancer. Caco-2 is a model of enterocytes that form an intestinal barrier-like layer.[69] Perhaps the $[Ru^{III}Cl_4(Nic)_2]^-[(CH_3)_2NH_2]^+$DMF complex, **1**, disrupts the integrity of this barrier or causes oxidative stress, which does not occur in other cell lines. However, it is worth noting that different ruthenium complexes exhibit different cytotoxic activity, suggesting that their structure could be further optimised to increase selectivity against cancer cells while reducing toxicity to healthy cells.[70–73] In our study, $[Ru^{III}Cl_2(3\text{-}HPA)_2]^-[3\text{-}HH_2PA]^+(EtOH)_2$ complex, **2**, showed a stronger ability to induce cell death compared to $[Ru^{III}Cl_4(Nic)_2]^-[(CH_3)_2NH_2]^+$DMF complex, **1**.

An inverted phase-contrast microscope was harnessed to evaluate the cell morphology after two days. Comparative images of L929 fibroblasts (Fig. 9), Hep-G2 cells (Fig. 10), and Caco-2 cells (Fig. 11) are shown for ruthenium complexes at concentrations of 0.1 and 0.025 mg ml^{-1} and for the controls performed. Comparative cell analysis confirmed the results obtained in the MTT test. Optical microscopy showed a toxic effect of DMSO at a concentration of 0.1% on L929 fibroblast cells. A damaged cell monolayer (rounded morphology compared to the untreated control) was then observed. A similar effect was noted for both ruthenium complexes at a concentration of 0.1%. L929 cells interacted with the $[Ru^{III}Cl_4(Nic)_2]^-[(CH_3)_2NH_2]^+$DMF complex, **1**, at a concentration of 0.025 mg ml^{-1}, contrary to the $[Ru^{III}Cl_2(3\text{-}HPA)_2]^-[3\text{-}HH_2PA]^+(EtOH)_2$ complex, **2**, treated cells, had an elongated shape, and their density was comparable to the control (Fig. 9), indicating their good viability. Hep-G2 cells show an epithelial-like morphology and initially attach in small patches of cells, which is very evident with the controls used and the $[Ru^{III}Cl_4(Nic)_2]^-[(CH_3)_2NH_2]^+$DMF complex, **1**. The $[Ru^{III}Cl_2(3\text{-}HPA)_2]^-[3\text{-}HH_2PA]^+(EtOH)_2$ complex, **2**, at concentrations of 0.01 and 0.025 mg ml^{-1} had a toxic effect on Hep-G2 cells, and it was observed that some of the cells rounded and shrank, while some retained a morphology similar to the control (Fig. 10). Caco-2 cells with healthy morphology form an epithelium-like monolayer with a transparent cytoplasm. This tendency was observed for cell controls without and with DMSO (especially for DMSO 0.025%). With both ruthenium complexes, the number of Caco-2 cells is lower than in the control sample, particularly at a complex concentration of 0.1 mg ml^{-1} (Fig. 11).

Anti-bacterial activity of $[Ru^{III}Cl_4(Nic)_2]^-[(CH_3)_2NH_2]^+$DMF and $[Ru^{III}Cl_2(3\text{-}HPA)_2]^-[3\text{-}HH_2PA]^+(EtOH)_2$ complexes

In the current study, *Klebsiella pneumoniae* strains were included as representative Gram-negative bacteria, which, according to the 2024 WHO Bacterial Priority Pathogens List, maintain the critical status, especially the carbapenemase-producing strains such as ATCC BAA-1705. Additionally, methicillin-resistant *Staphylococcus aureus* (MRSA) strains represent the high-priority group. We also included non-resistant reference strains from the ATCC collection to ensure a comprehensive comparison. Furthermore, clinical isolates obtained from diabetic foot ulcers were analysed. These samples are vital since diabetic foot infections are recognised as a major driver of multidrug resistance emergence. According to literature data, most bacterial strains isolated from this type of chronic wound exhibit multidrug resistance, making their treatment especially challenging.[74]

Fig. 12 shows the results of the bactericidal properties studies of the $[Ru^{III}Cl_4(Nic)_2]^-[(CH_3)_2NH_2]^+$DMF complex, **1**. In the case of all the tested bacteria, no complete inhibition of growth was observed. In the case of Gram-positive bacteria, *S. aureus*, only for strain ATCC BAA-1026, there was a slight decrease in viability at all concentrations, accounting for about 20%. For strains B5 and ATCC 29213, although variations in viability are apparent on the graph, considering the standard deviations, no significant differences in viability were observed. In the case of Gram-negative bacteria *K. pneumoniae*, ATCC BAA-1705, no substantial change in viability was observed. Instead, for strain B34 at the highest concentration of **1**, a decrease of nearly 45% can be distinguished. For ATCC

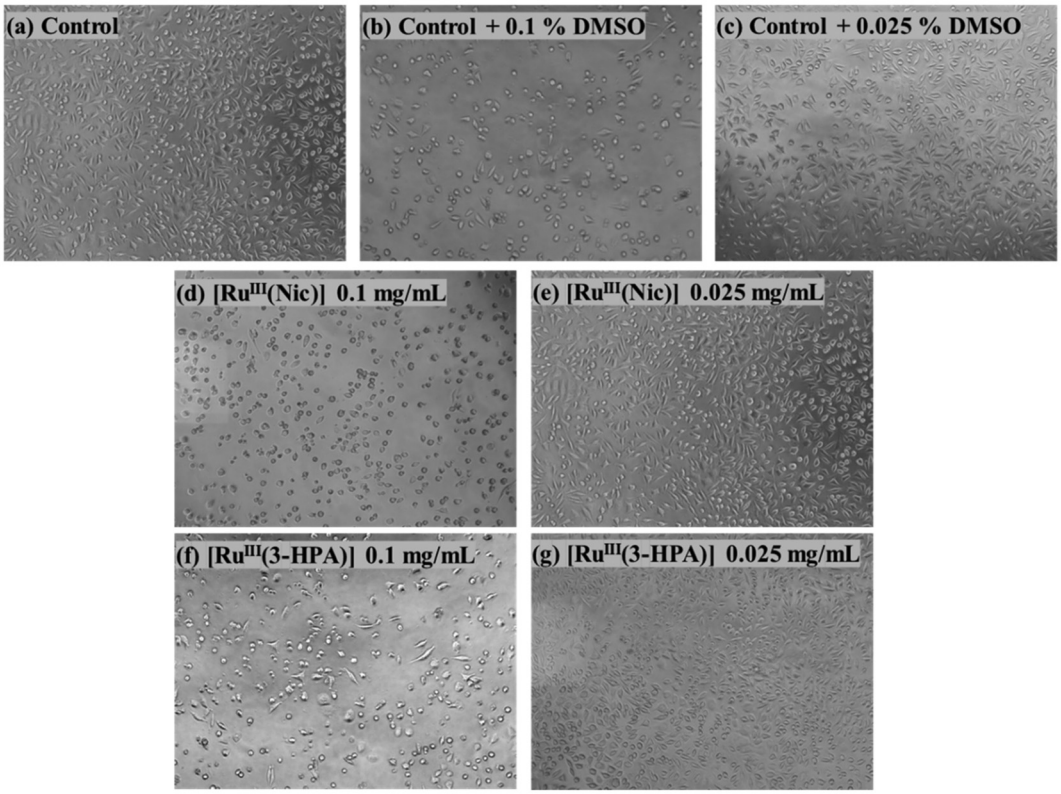

Fig. 9 Images of L929 fibroblasts growing on (a) the control, (b and c) control with DMSO, (d and e) $[Ru^{III}Cl_4(Nic)_2]^-[(CH_3)_2NH_2]^+$DMF and (f and g) $[Ru^{III}Cl_2(3\text{-}HPA)_2]^-[3\text{-}HH_2PA]^+(EtOH)_2$ for two days. The type and concentration of specimens are presented in the figures.

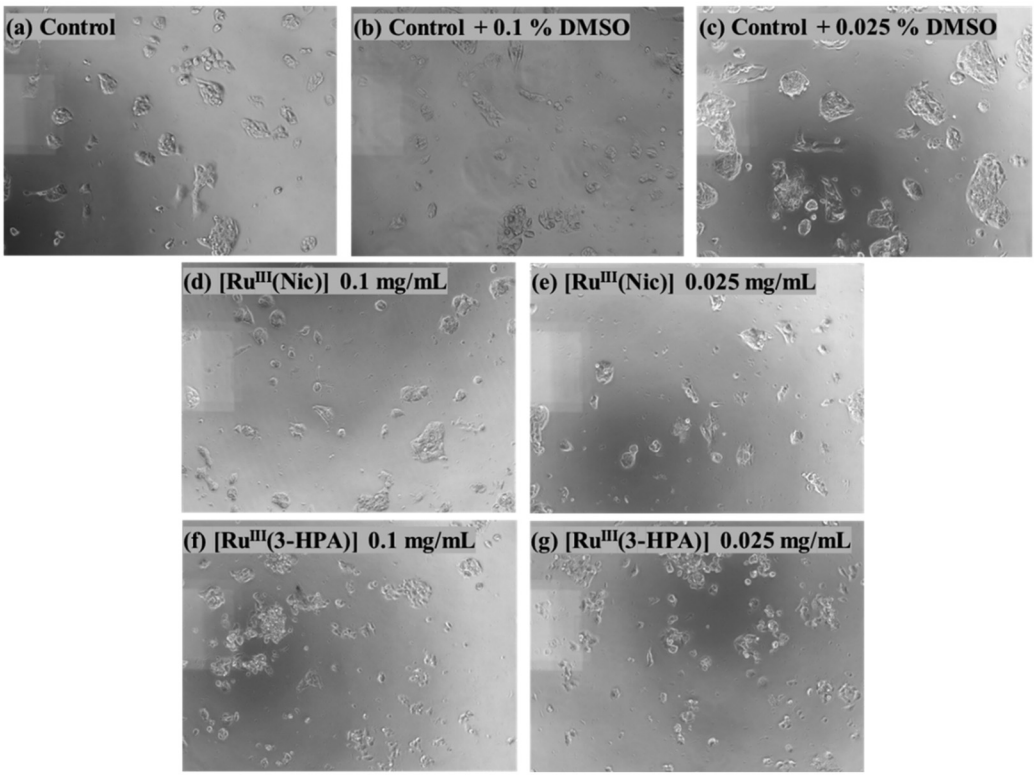

Fig. 10 Images of Hep-G2 cells growing on (a) the control, (b and c) control with DMSO, (d and e) $[Ru^{III}Cl_4(Nic)_2]^-[(CH_3)_2NH_2]^+$DMF and (f and g) $[Ru^{III}Cl_2(3\text{-}HPA)_2]^-[3\text{-}HH_2PA]^+(EtOH)_2$ for two days. The type and concentration of specimens are presented in the figures.

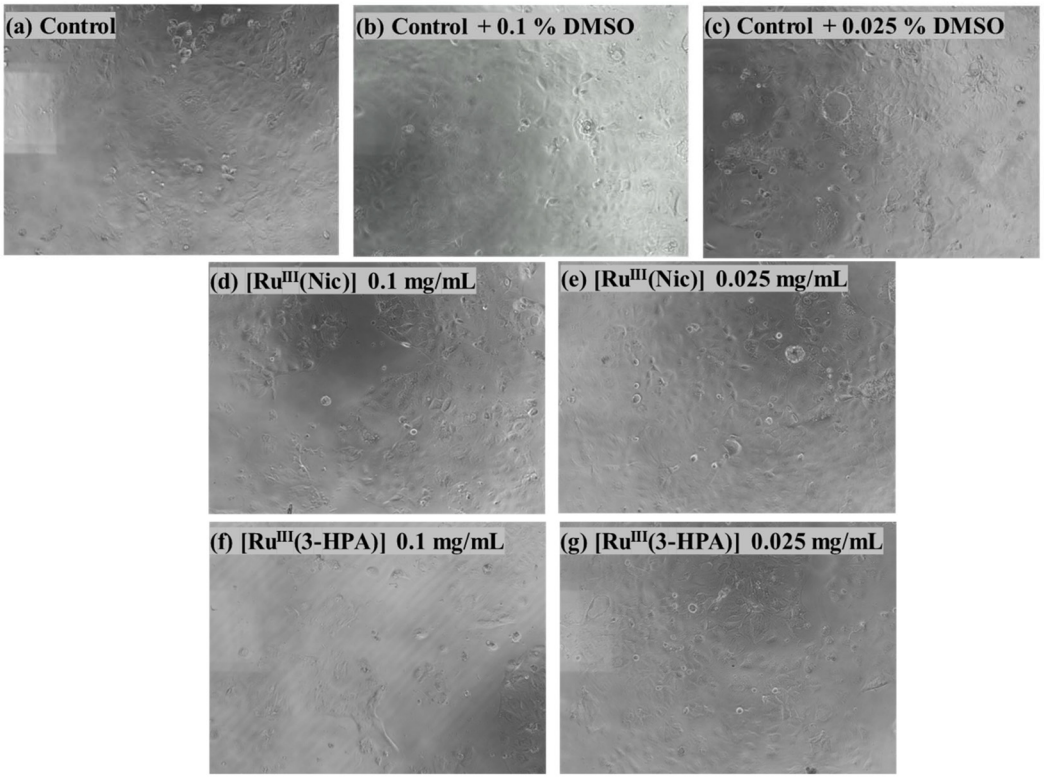

Fig. 11 Images of Caco-2 cells growing on (a) the control, (b and c) control with DMSO, (d and e) $[Ru^{III}Cl_4(Nic)_2]^-[(CH_3)_2NH_2]^+$DMF and (f and g) $[Ru^{III}Cl_2(3\text{-}HPA)_2]^-[3\text{-}HH_2PA]^+(EtOH)_2$ for two days. The type and concentration of specimens are presented in the figures.

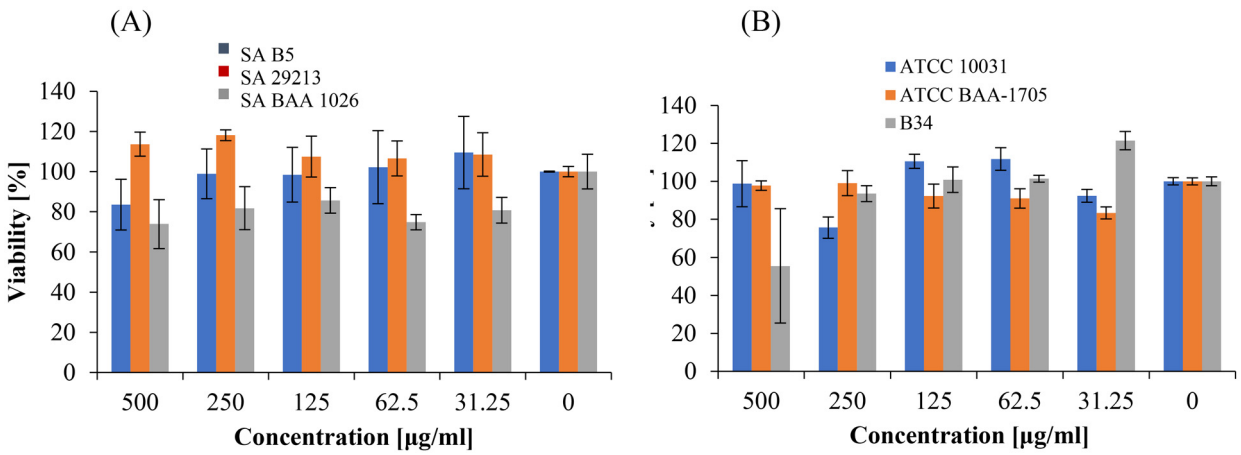

Fig. 12 Bacterial viability results for (A) *S. aureus* ATCC BAA-1026, ATCC 29213, B5 strains and (B) *K. pneumonia* ATCC BAA-1705, ATCC 10031, B34 strains treated with $[Ru^{III}Cl_4(Nic)_2]^-[(CH_3)_2NH_2]^+$DMF complex.

10031, a comparable decrease is also observed at a concentration of 250 µg ml^{-1}, while for B34, at a concentration of 31.25 µg ml^{-1}, there was an improvement in viability by about 20%.

The bactericidial properties of $[Ru^{III}Cl_2(3\text{-}HPA)_2]^-[3\text{-}HH_2PA]^+(EtOH)_2$ are illustrated in Fig. 13. It can be seen that complex **2** has higher antibacterial potential than complex **1** for all tested strains. In the case of *K. pneumoniae* strains ATCC 10031, ATCC BAA-1705 and B34 at the concentration of 500 µg ml^{-1}, the reduction in viability accounted for 10, 20 and 60%, respectively. Instead, *S. aureus* reveals higher sensitivity to the tested compound. Reduced viability was observed already at 125 µg ml^{-1} concentration for strains ATCC 29213 and ATCC BAA-1026. The B5 strain maintained viability across all concentrations except at 500 µg ml^{-1}, where survival dropped to 7%. At the same concentration, the survival rate for the ATCC

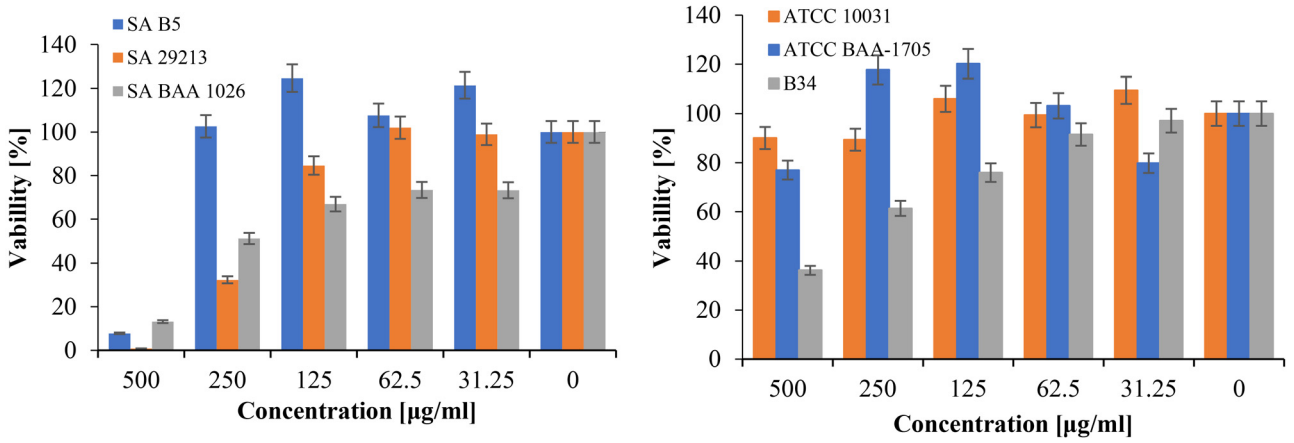

Fig. 13 Bacterial viability results for (A) *S. aureus* ATCC BAA-1026, ATCC 29213, B5 strains and (B) *K. pneumonia* ATCC BAA-1705, ATCC 10031, B34 strains treated with $[Ru^{III}Cl_2(3\text{-HPA})_2]^-[3\text{-}HH_2PA]^+(EtOH)_2$ for complex.

BAA-1026 strain was 13%, while for ATCC 29213, it was approximately 0%, demonstrating that the MIC was reached. The results would indicate the potential of using the synthesised complex to combat infections caused by Gram-positive bacteria such as *S. aureus*. However, its higher toxicity towards healthy cells (fibroblasts tested) than Gram-positive bacteria precludes considering this compound as a potential antibacterial agent or requires optimisation of its toxic selectivity.

The studies on Ru-containing complexes revealed that the bactericidal properties depend on the supporting ligand, and the obtained MIC is comparable to the previously obtained results (*i.e.* 1500 µg ml^{-1} depending on the tested strains and compounds).[75–78] One less investigated aspect in the current scientific literature is the precise mechanism of ruthenium complexes' action underlying their biological activity. Proposed mechanisms often highlight the potential for ruthenium or its accompanying ligands to interact with DNA, disrupting cellular functions. However, a comprehensive understanding of these processes remains elusive and warrants further investigation. Some other studies, such as those published by Lam *et al.*, claimed that the plausible mechanism involves generating reactive oxygen species (ROS) during incubation with bacteria. The respective was demonstrated to be relevant for enhanced antimicrobial activity of $[Ru^{II}(L_1)_2(L_2)]^{2+}$ complexes for L_2 = *N*-phenyl-substituted diazafluorene ligands against MRSA strains.[79]

On the other hand, the studies on $[Ru(pic)_3]^0$ complexes' activity against *K. pneumoniae* and *S. aureus* strains revealed unexpected results. Despite its toxic effects on all studied strains, no ROS generation was observed, and a significant reduction in the natural ROS level was detected. It suggests that ruthenium may impair the bacterial respiratory chain.[79] This effect may be due to its ability to mimic iron, the vital cofactor of cytochromes and other cytochrome-type oxidases,[79] while unable to replace its essential function. Current studies indicate that nicotinamide, a part of the NAD^+ cofactor that takes part in a respiratory chain, can counteract the adverse effects of ruthenium. Previous work has shown that nicotinamide riboside can enhance the energy of complex **I–II** of the respiratory chains,[80] which supports our suggestions on the possible involvement of ruthenium in such metabolic routes.

Summary and conclusions

In this study, two novel ruthenium(III) complexes, $[Ru^{III}Cl_4(Nic)_2]^-[(CH_3)_2NH_2]^+DMF$, **1**, and $[Ru^{III}Cl_2(3\text{-HPA})_2]^-[3\text{-}HH_2PA]^+(EtOH)_2$, **2**, were synthesised and characterised. Comprehensive structural analysis confirmed that complex **1** crystallises in a monoclinic *C*2/*c* space group with a distorted octahedral geometry, while complex **2** adopts a triclinic $P\bar{1}$ space group with a comparable coordination environment. X-ray diffraction, spectroscopic studies, and elemental analysis provided detailed insight into their molecular structures and stability. These complexes' micro- and nanoparticles (NPs) were synthesised using the LASC method to explore their potential applications further. SEM and DLS analyses confirmed successful nanoparticle formation, with hydrodynamic diameters ranging from 47 to 375 nm, depending on the synthesis conditions. The preparation method (magnetic stirring *vs.* sonication) influenced particle morphology and size distribution, yielding more uniform spherical particles, while sonication produced elongated and aggregated structures. XRD studies confirmed high crystallinity, and crystallite size calculations using the Williamson–Hall and Scherrer methods indicated sizes of approximately 15 and 18 nm for **1** and 8.92 and 24.22 nm for **2**, respectively. The investigated ruthenium(III) complexes formed dispersive systems with limited colloidal stability and a strong tendency to aggregate; their behaviour is highly sensitive to both concentration and environment. This significant variability in aggregation profiles and zeta potential values indicates that steric, hydrophobic, and biomolecular interactions with medium components play a decisive role in

determining their behaviour and potential biological activity beyond electrostatic forces.

The antimicrobial activity assessment of the studied complexes against clinically relevant bacterial strains revealed that complex **2**, featuring the 3-hydroxypicolinate ligand, exhibits significantly higher bactericidal efficacy than complex **1**, containing nicotinic acid. Complex **2** demonstrates a MIC value of 125 μg mL^{-1} against methicillin-resistant *Staphylococcus aureus* (MRSA) strains, while complex **1** displays limited antimicrobial activity. These findings suggest that the ligand environment modulates biological activity, with 3-hydroxypicolinate enhancing antibacterial effects. Mechanistic investigations indicate that the antimicrobial action of these ruthenium complexes may involve reactive oxygen species (ROS) generation and disruption of bacterial respiratory chain functions. Interestingly, nicotinic acid in complex **1** appears to mitigate oxidative stress, whereas the 3-hydroxypicolinate ligands in complex **2** contribute to enhanced bioactivity. These observations align with previous studies on ruthenium-based antimicrobial agents, reinforcing the role of ligand chemistry in dictating biological efficacy. Similarly, the presented data indicate an essential impact of a coordination sphere composition on the cytotoxicity towards host cells. The $[Ru^{III}Cl_2(3\text{-}HPA)_2]^-[3\text{-}HH_2PA]^+(EtOH)_2$ complex, **2**, is markedly cytotoxic, while $[Ru^{III}Cl_4(Nic)_2]^-[(CH_3)_2NH_2]^+$DMF species, **1**, at a concentration of 0.025 mg ml^{-1}, is a promising anti-cancer drug candidate targeting intestinal cancers, showing cytotoxicity against Caco-2 cancer cells and no cytotoxicity against L929 fibroblasts cells. Since nanoparticles often exhibit distinct biological behaviours compared to their molecular counterparts, including altered cellular uptake, distribution, and toxicity profiles, we will address the biological effects of the reported **NPs(1)** and **NPs(2)** in future studies. The planned research will also focus on optimising nanoparticle stability and delivery to target cells, potentially enhancing the selectivity and efficacy of ruthenium complexes as therapeutic agents. However, evaluating their bioactivity requires the development of dedicated dispersion protocols to ensure reproducibility and stability in cell culture media, which differ substantially from solvents used in physicochemical characterisation.

Author contributions

Olga Impert: Experimentation and formal data analysis, conceptualisation, coordination of experimental work, writing – original draft, review & editing. Oleksandra Pryshchepa: Biological studies. Paweł Pomastowski: Biological studies, formal analysis. Michalina Ehlert: Biological studies, DLS, formal analysis. Natalia Czerniecka: Biological studies. Natalia Balińska: Biological studies. Barbara Kubiak: Preparation of NPs. Anna Kozakiewicz-Piekarz: X-ray crystallography. Maciej Witwicki: EPR and DFT calculations. Yogeswara Rao Pateda: Theoretical calculations. Erik Rakovský: Theoretical calculations. Anna Katafias: Review & editing. Rudi van Eldik: Review & editing.

Conflicts of interest

There are no conflicts to declare.

Data availability

The data supporting this article have been included as part of the SI. See DOI: **https://doi.org/10.1039/d5dt01857a**.

Solubility of $[Ru^{III}Cl_4(Nic)_2]^-[(CH_3)_2NH_2]^+$DMF, **1**, and $[Ru^{III}Cl_2(3\text{-}HPA)_2]^-[3\text{-}HH_2PA]^+(EtOH)_2$, **2**, complexes in selected solvents, X-ray data, EDX patterns, and SEM images, IR spectra for **1** and **2**, additional DFT data, crystallite sizes and elastic strains, hydrodynamic sizes and SEM images, Williamson-Hall plots for NPs(1) and NPs(2), hydrodynamic size and zeta potential of **1** and **2** in aqueous and biological media, cytotoxic data.

CCDC 2401926 and 2401927 contain the supplementary crystallographic data for this paper.[81a,b]

Acknowledgements

The National Science Centre financially supported this work, research project no. 2020/37/B/ST4/01082. Nicolaus Copernicus University in Toruń financially supported this work as part of the IDUB UMK program (Debuts VIII). The authors kindly acknowledge the support of Klaudia Wesołowska (IR) and Aleksandra Cyganiuk (X-ray powder diffraction). The DFT computations were performed using resources provided by the Wroclaw Centre for Networking and Supercomputing (**https://wcss.pl**). Paweł Pomastowski and Oleksandra Pryshchepa are members of the Toruń Centre of Excellence "Towards Personalised Medicine" operating under the Excellence Initiative Research University.

References

1 N. A. Turner, B. K. Sharma-Kuinkel, S. A. Maskarinec, E. M. Eichenberger, P. P. Shah, M. Carugati, T. L. Holland and V. G. Fowler Jr., Methicillin-resistant Staphylococcus aureus: an overview of basic and clinical research, *Nat. Rev. Microbiol.*, 2019, **17**, 203.

2 M. Złoch, P. Pomastowski, M. Peer, K. Sparbier, M. Kostrzewa and B. Buszewski, Study on carbapenemase-producing bacteria by matrix-assisted laser desorption/ionisation approach, *PLoS One*, 2021, **16**(3), e0247369.

3 J. E. Waters, L. Stevens-Cullinane, L. Siebenmann and J. Hess, Recent advances in the development of metal complexes as antibacterial agents with metal-specific modes of action, *Curr. Opin. Microbiol.*, 2023, **75**, 102347.

4 P. Thangavell, B. Viswanath and K. Kim, Recent developments in the nanostructured materials functionalised with ruthenium complexes for targeted drug delivery to tumours, *Int. J. Nanomed.*, 2017, **12**, 2749.

5 S. Thakur, A. Jarya and A. Bhalla, Recent advances in biological and medicinal profile of Schiff bases and their

metal complexes: An updated version (2018–2023), *Results Chem.*, 2024, **7**, 101350.
6 C. Metcalfe and J. A. Thomas, Kinetically inert transition metal complexes that reversibly bind to DNA, *Chem. Soc. Rev.*, 2003, **32**, 215.
7 B. M. Zeglis, V. C. Pierre and J. K. Barton, Metallo-intercalators and metallo-insertors, *Chem. Commun.*, 2007, **44**, 4565.
8 F. R. Keene, J. A. Smith and J. G. Collins, Metal complexes as structure-selective binding agents for nucleic acids, *Coord. Chem. Rev.*, 2009, **253**, 2021.
9 M. R. Gill and J. A. Thomas, Ruthenium(II) polypyridyl complexes and DNA-from structural probes to cellular imaging and therapeutics, *Chem. Soc. Rev.*, 2012, **41**, 3179.
10 C. A. Puckett and J. K. Barton, Mechanism of cellular uptake of a ruthenium polypyridyl complex, *Biochemistry*, 2008, **47**, 11711.
11 C. Shobha Devi, D. Anil Kumar, S. S. Singh, N. Gabra, N. Deepika, Y. Praveen Kumar and S. Satyanarayana, Synthesis, interaction with DNA, cytotoxicity, cell cycle arrest and apoptotic inducing properties of ruthenium(II) molecular "light switch" complexes, *Eur. J. Med. Chem.*, 2013, **64**, 410.
12 F. P. Dwyer, E. C. Gyarfas, W. P. Rogers and J. H. Koch, Biological activity of complex ions, *Nature*, 1952, **170**, 190.
13 A. Bolhuis, L. Hand, J. E. Marshall, A. D. Richards, A. Rodger and J. Aldrich-Wright, Antimicrobial activity of ruthenium-based intercalators, *Eur. J. Pharm. Sci.*, 2011, **42**, 313.
14 P. L. Lam, G. L. Lu, K. M. Hon, K. W. Lee, C. L. Ho, X. Wang, J. C. O. Tang, K. H. Lam, R. S. M. Wong, S. H. L. Kok, Z. X. Bian, H. Li, K. K. H. Lee, R. Gambari, C. H. Chui and W. Y. Wong, Development of ruthenium(II) complexes as topical antibiotics against methicillin-resistant Staphylococcus aureus, *Dalton Trans.*, 2014, **43**, 3949.
15 M. J. Hajipour, K. M. Fromm, A. A. Ashkarran, D. Jimenez de Aberasturi, I. R. de Larramendi, T. Rojo, V. Serpooshan, W. J. Parak and M. Mahmoudi, Antibacterial properties of nanoparticles, *Trends Biotechnol.*, 2012, **30**, 499.
16 A. Gupta, S. Mumtaz, C. H. Hussain, I. Li and V. M. Rotello, Combatting antibiotic-resistant bacteria using nanomaterials, *Chem. Soc. Rev.*, 2019, **48**, 415.
17 N. Sanvicens and M. P. Marco, Multifunctional nanoparticles – properties and prospects for their use in human medicine, *Trends Biotechnol.*, 2008, **26**, 425.
18 X. Zhu, A. F. Radovic-Moreno, J. Wu, R. Langer and J. Shi, Nanomedicine in the management of microbial infection – overview and perspectives, *Nano Today*, 2014, **9**, 478.
19 Y. Chen, L. Liu, X. Wang, Z. Liao, R. Wang, Y. Xiong, J. Cheng, G. Jiang, J. Wang and X. Liao, *Dalton Trans.*, 2022, **51**, 14980.
20 C. S. Allardyce and P. J. Dyson, Ruthenium in medicine: current clinical uses and future prospects, *Platinum Met. Rev.*, 2001, **45**, 62.
21 *CrysAlis 171.38.43 package of programs*, Rigaku Oxford Diffraction, 2015.
22 G. M. Sheldrick, *Acta Crystallogr., Sect. C: Struct. Chem.*, 2015, **71**, 3.
23 S. Stoll and A. Schweiger, EasySpin, a Comprehensive Software Package for Spectral Simulation and Analysis in EPR, *J. Magn. Reson.*, 2006, **178**, 42.
24 S. Stoll, CW-EPR Spectral Simulations, in *Methods in Enzymology*, Academic Press, 2015, vol. 563, p. 121.
25 F. Neese, F. Wennmohs, U. Becker and C. Riplinger, The ORCA Quantum Chemistry Program Package, *J. Chem. Phys.*, 2020, **152**, 224108.
26 F. Neese, The ORCA Program System, *Wiley Interdiscip. Rev.: Comput. Mol. Sci.*, 2012, **2**, 73.
27 F. Neese, Software Update: The ORCA Program System—Version 5.0, *Wiley Interdiscip. Rev.: Comput. Mol. Sci.*, 2022, **12**, e1606.
28 C. van Wüllen, Molecular Density Functional Calculations in the Regular Relativistic Approximation: Method, Application to Coinage Metal Diatomics, Hydrides, Fluorides and Chlorides, and Comparison with First-Order Relativistic Calculations, *J. Chem. Phys.*, 1998, **109**, 392.
29 J. D. Rolfes, F. Neese and D. A. Pantazis, All-Electron Scalar Relativistic Basis Sets for the Elements Rb–Xe, *J. Comput. Chem.*, 2020, **41**, 1842.
30 D. A. Pantazis, X.-Y. Chen, C. R. Landis and F. Neese, All-Electron Scalar Relativistic Basis Sets for Third-Row Transition Metal Atoms, *J. Chem. Theory Comput.*, 2008, **4**, 908.
31 F. Weigend and R. Ahlrichs, Balanced Basis Sets of Split Valence, Triple Zeta Valence and Quadruple Zeta Valence Quality for H to Rn: Design and Assessment of Accuracy, *Phys. Chem. Chem. Phys.*, 2005, **7**, 3297.
32 F. Neese, An Improvement of the Resolution of the Identity Approximation for the Formation of the Coulomb Matrix, *J. Comput. Chem.*, 2003, **24**, 1740.
33 F. Neese, F. Wennmohs, A. Hansen and U. Becker, Efficient, Approximate and Parallel Hartree–Fock and Hybrid DFT Calculations. A 'Chain-of-Spheres' Algorithm for the Hartree–Fock Exchange, *Chem. Phys.*, 2009, **356**, 98.
34 F. Weigend, Accurate Coulomb-Fitting Basis Sets for H to Rn, *Phys. Chem. Chem. Phys.*, 2006, **8**, 1057.
35 J. Tao, J. P. Perdew, V. N. Staroverov and G. E. Scuseria, Climbing the Density Functional Ladder: Nonempirical Meta–Generalised Gradient Approximation Designed for Molecules and Solids, *Phys. Rev. Lett.*, 2003, **91**, 146401.
36 F. Neese, Prediction of Electron Paramagnetic Resonance *g* Values Using Coupled Perturbed Hartree–Fock and Kohn–Sham Theory, *J. Chem. Phys.*, 2001, **115**, 11080.
37 F. Neese, Efficient and Accurate Approximations to the Molecular Spin-Orbit Coupling Operator and Their Use in Molecular g-Tensor Calculations, *J. Chem. Phys.*, 2005, **122**, 034107.
38 C. Adamo and V. Barone, Toward Reliable Density Functional Methods without Adjustable Parameters: The PBE0 Model, *J. Chem. Phys.*, 1999, **110**, 6158.
39 A. D. Becke, A New Mixing of Hartree–Fock and Local Density-Functional Theories, *J. Chem. Phys.*, 1993, **98**, 1372.
40 S. Grimme, Accurate Calculation of the Heats of Formation for Large Main Group Compounds with Spin-Component Scaled MP2 Methods, *J. Phys. Chem. A*, 2005, **109**, 3067.

41 M. M. Quintal, A. Karton, M. A. Iron, A. D. Boese and J. M. L. Martin, Benchmark Study of DFT Functionals for Late-Transition-Metal Reactions, *J. Phys. Chem. A*, 2006, **110**, 709.
42 A. Allouche, Gabedit—A Graphical User Interface for Computational Chemistry Softwares, *J. Comput. Chem.*, 2011, **32**, 174.
43 O. Impert, O. Pryshchepa, P. Pomastowski, K. Rafińska and D. Chatterjee, Redox reaction of a RuIII(pic)$_3$ complex with cysteine: Spectral, kinetic and biological studies, *Inorg. Chim. Acta*, 2025, **574**, 122401.
44 O. Impert, A. Kozakiewicz-Piekarz, A. Katafias, M. Witwicki, U. K. Komarnicka, K. Kurpiewska and R. van Eldik, Mixed-valence outer-sphere RuII/RuIII ion-pair complexes. Synthesis, experimental, and theoretical studies, *Polyhedron*, 2022, **223**, 115939.
45 I. Fleming and D. Williams, *Spectroscopic Methods in Organic Chemistry*, Springer Nature Switzerland AG, 7th edn, 2019, p. 111.
46 J. A. Weil and J. R. Bolton, *Electron Paramagnetic Resonance: Elementary Theory and Practical Applications*, Wiley-Interscience, Hoboken, N.J., 2nd edn, 2007.
47 N. Cetinbas, M. I. Webb, J. A. Dubland and C. J. Walsby, Serum-Protein Interactions with Anti-cancer Ru(III) Complexes KP1019 and KP418 Characterised by EPR, *J. Biol. Inorg. Chem.*, 2010, **15**, 131.
48 E. Tfouni, F. G. Doro, A. J. Gomes, R. S. D. Silva, G. Metzker, P. G. Z. Benini and D. W. Franco, Immobilised Ruthenium Complexes and Aspects of Their Reactivity, *Coord. Chem. Rev.*, 2010, **254**, 355.
49 M. M. T. Khan, D. Srinivas, R. I. Kureshy and N. H. Khan, Synthesis, Characterisation, and EPR Studies of Stable Ruthenium(III) Schiff Base Chloro and Carbonyl Complexes, *Inorg. Chem.*, 1990, **29**, 2320.
50 M. L. Souza, E. E. Castellano, J. Telser and D. W. Franco, Secondary Coordination Sphere Effects in Ruthenium(III) Tetraammine Complexes: Role of the Coordinated Water Molecule, *Inorg. Chem.*, 2015, **54**, 2067.
51 O. K. Medhi and U. Agarwala, Electron Spin Resonance Studies of Some Ruthenium(III) Complexes, *Inorg. Chem.*, 1980, **19**, 1381.
52 M. I. Webb and C. J. Walsby, Albumin Binding and Ligand-Exchange Processes of the Ru(iii) Anti-cancer Agent NAMI-A and Its Bis-DMSO Analogue Determined by ENDOR Spectroscopy, *Dalton Trans.*, 2015, **44**, 17482.
53 B. R. McGarvey, Survey of Ligand Field Parameters of Strong Field D5 Complexes Obtained from the g Matrix, *Coord. Chem. Rev.*, 1998, **170**, 75.
54 B. R. McGarvey, The ESR g Matrix for Strong Field D5 Systems, *Quim. Nova*, 1998, **21**, 206.
55 O. Impert, A. Kozakiewicz, G. Wrzeszcz, A. Katafias, A. Bieńko, R. van Eldik and A. Ozarowski, Characterization of a Mixed-Valence Ru(II)/Ru(III) Ion-Pair Complex. Unexpected High-Frequency Electron Paramagnetic Resonance Evidence for Ru(III)–Ru(III) Dimer Coupling, *Inorg. Chem.*, 2020, **59**, 8609.
56 V. T. Coombe, G. A. Heath, T. A. Stephenson and D. A. Tocher, Electrochemical One-Electron Oxidation of $[Ru(NO)Cl_5]^{2-}$: Spectroscopic and Magnetic Evidence for the (t_{2g}^5) Ruthenium(III) Pentachloronitrosyl Complex Monoanion $[Ru(NO)Cl_5]^-$, *J. Chem. Soc., Chem. Commun.*, 1983, 303.
57 W. M. Reiff and R. E. DeSimone, Electronic Ground States of Dicyanobis(Diimine)Iron(III) Compounds, *Inorg. Chem.*, 1973, **12**, 1793.
58 P. Pomastowski, M. Sprynskyy, P. Žuvela, K. Rafińska, M. Milanowski, J. Jay Liu, M. Yi and B. Buszewski, Silver-Lactoferrin Nanocomplexes as a Potent Antimicrobial Agent, *J. Am. Chem. Soc.*, 2016, **138**, 7899.
59 P. Pomastowski and B. Buszewski, Influence of heterogeneity biocolloids surface on their electrophoretic separation, *Wiad. Chem.*, 2015, **69**, 823.
60 S. Narimatsu, N. Takatsu, S. Yamano, Y. Inoue, N. Hanioka, K. Kiryu, S. Naito, F. J. Gonzalez and S. Yamamoto, The Effect of Dimethyl Sulfoxide on the Function of Cytochrome P450 2D6 in HepG2 Cells upon the Co-Expression with NADPH-Cytochrome P450 Reductase, *Chem.-Biol. Interact.*, 2006, **159**, 47.
61 R. Notman, M. Noro, B. O'Malley and J. Anwar, Molecular Basis for Dimethylsulfoxide (DMSO) Action on Lipid Membranes, *J. Am. Chem. Soc.*, 2006, **128**, 13982.
62 F. He, W. Liu, S. Zheng, L. Zhou, B. Ye and Z. Qi, Ion Transport through Dimethyl Sulfoxide (DMSO) Induced Transient Water Pores in Cell Membranes, *Mol. Membr. Biol.*, 2012, **29**, 107.
63 A. B. Becceneri, M. Fuzer, A. C. Lopes, P. B. da Silva, A. M. Plutin, A. A. Batista, M. Chorilli and M. R. Cominetti, Nanoencapsulation of Ruthenium Complex Ru(ThySMet): A Strategy to Improve Selective Cytotoxicity against Breast Tumor Cells in 2D and 3D Culture Models, *Curr. Drug Discovery Technol.*, 2024, **21**, 33.
64 C. Irace, G. Misso, A. Capuozzo, M. Piccolo, C. Riccardi, A. Luchini, M. Caraglia, L. Paduano, D. Montesarchio and R. Santamaria, Antiproliferative Effects of Ruthenium-Based Nucleolipidic Nanoaggregates in Human Models of Breast Cancer in Vitro: Insights into Their Mode of Action, *Sci. Rep.*, 2017, **7**, 45236.
65 J. Shen, H. C. Kim, J. Wolfram, C. Mu, W. Zhang, H. Liu, Y. Xie, J. Mai, H. Zhang, Z. Li, M. Guevara, Z. W. Mao and H. A. Shen, A Liposome Encapsulated Ruthenium Polypyridine Complex as a Theranostic Platform for Triple-Negative Breast Cancer, *Nano Lett.*, 2017, **17**, 2913.
66 L. Chen, C. Fu, Y. Deng, W. Wu and A. Fu, A pH-Sensitive Nanocarrier for Tumor Targeting, *Pharm. Res.*, 2016, **33**, 2989.
67 C. C. Wee, M. B. Hamel, R. B. Davis and R. S. Phillips, Assessing the Value of Weight Loss among Primary Care Patients, *J. Gen. Intern. Med.*, 2004, **19**, 1206–1211.
68 G. Süss-Fink, Areneruthenium Complexes as Anti-cancer Agents, *Dalton Trans.*, 2010, **39**, 1673–1688.
69 I. J. Hidalgo, T. J. Raub and R. T. Borchardt, Characterization of the Human Colon Carcinoma

Cell Line (Caco-2) as a Model System for Intestinal Epithelial Permeability, *Gastroenterology*, 1989, **96**, 736–749.

70 M. Savic, A. Arsenijevic, J. Milovanovic, B. Stojanovic, V. Stankovic, A. Rilak Simovic, D. Lazic, N. Arsenijevic and M. Milovanovic, Anti-tumor Activity of Ruthenium(II) Terpyridine Complexes towards Colon Cancer Cells In Vitro and In Vivo, *Molecules*, 2020, **25**, 4699.

71 A. P. Lima, F. C. Pereira, M. A. P. Almeida, F. M. S. Mello, W. C. Pires, T. M. Pinto, F. K. Delella, S. L. Felisbino, V. Moreno, A. A. Batista and P. Silveira-Lacerda, Cytoxicity and Apoptotic Mechanism of Ruthenium(II) Amino Acid Complexes in Sarcoma-180 Tumor Cells, *PLoS One*, 2014, **9**, 10.

72 M. Fandzloch, L. Dobrzańska, T. Jędrzejewski, J. Jezierska, J. Wiśniewska and I. Łakomska, Synthesis, Structure and Biological Evaluation of Ruthenium(III) Complexes of Triazolopyrimidines with Anticancer Properties, *J. Biol. Inorg. Chem.*, 2020, **25**, 109–124.

73 S. Kapitza, M. Pongratz, M. A. Jakupec, P. Heffeter, W. Berger, L. Lackinger, B. K. Keppler and B. Marian, Heterocyclic Complexes of Ruthenium(III) Induce Apoptosis in Colorectal Carcinoma Cells, *J. Cancer Res. Clin. Oncol.*, 2005, **131**, 101–110.

74 X. Yan, J. Song, L. Zhang and X. Li, Analysis of risk factors for multidrug-resistant organisms in diabetic foot infection, *BMC Endocr. Disord.*, 2022, **22**, 46.

75 P. Rogala, G. Czerwonka, S. Michałkiewicz, M. Hodorowicz, B. Barszcz and A. Jabłońska-Wawrzycka, Synthesis, Structural Characterization and Antimicrobial Evaluation of Ruthenium Complexes with Heteroaromatic Carboxylic Acids, *Chem. Biodivers.*, 2019, **16**, e1900403.

76 J. Marques, T. M. Braga, F. A. Almeida Paz, T. M. Santos, M. de Fátima Silva Lopes and S. S. Braga, Cyclodextrins improve the antimicrobial activity of the chloride salt of Ruthenium(II) chloro-phenanthroline-trithiacyclononane, *BioMetals*, 2009, **22**, 541.

77 K. Ashwini Kumar, K. L. Reddy, S. Vidhisha and S. Satyanarayana, Synthesis, characterisation and DNA binding and photocleavage studies of $[Ru(bpy)_2BDPPZ]^{2+}$, $[Ru(dmb)_2BDPPZ]^{2+}$ and $[Ru(phen)_2BDPPZ]^{2+}$ complexes and their antimicrobial activity, *Appl. Organomet. Chem.*, 2009, **23**, 409.

78 P. L. Lam, G. L. Lu, K. M. Hon, K. W. Lee, C. L. Ho, X. Wang, J. C. O. Tang, K. H. Lam, R. S. M. Wong, S. H. L. Kok, Z. X. Bian, H. Li, K. K. H. Lee, R. Gambari, C. H. Chui and W. Y. Wong, Development of ruthenium(II) complexes as topical antibiotics against methicillin-resistant Staphylococcus aureus, *Dalton Trans.*, 2014, **43**, 3949.

79 V. R. I. Kaila and M. Wikström, Architecture of bacterial respiratory chains, *Nat. Rev. Microbiol.*, 2021, **19**, 319.

80 R. Pawlosky, T. G. Demarest, M. T. King, D. Estrada, R. L. Veech and V. A. Bohr, Effect of Dietary Ketosis and Nicotinamide Riboside on Hippocampal Krebs Cycle Intermediates and Mitochondrial Energetics in a DNA Repair-Deficient 3xTg/POL$\beta^{+/-}$ Alzheimer Disease Mouse Model, *J. Neurochem.*, 2025, **169**, e16295.

81 (*a*) A. Kozakiewicz-Piekarz, CCDC 2401926 for $[Ru^{III}Cl_4(Nic)_2]^-[(CH_3)_2NH_2]^+DMF$ (compound **1**): Experimental Crystal Structure Determination, 2024, DOI: **10.5517/ccdc.csd.cc2lmdh4**; (*b*) A. Kozakiewicz-Piekarz, CCDC 2401927 for $[Ru^{III}Cl_2(3\text{-}HPA)_2]^-[3\text{-}HH_2PA]^+(EtOH)_2$ (compound **2**): Experimental Crystal Structure Determination, 2024, DOI: **10.5517/ccdc.csd.cc2lmdj5**.